BABAR-PUB-08/045
SLAC-PUB-13437
hep-ex/xxxx

arXiv:0811.0564v1 [hep-ex] 4 Nov 2008

Search for the $Z(4430)^-$ at *BABAR*

B. Aubert, M. Bona, Y. Karyotakis, J. P. Lees, V. Poireau, E. Prencipe, X. Prudent, and V. Tisserand
Laboratoire de Physique des Particules, IN2P3/CNRS et Université de Savoie, F-74941 Annecy-Le-Vieux, France

J. Garra Tico and E. Grauges
Universitat de Barcelona, Facultat de Fisica, Departament ECM, E-08028 Barcelona, Spain

L. Lopez[ab], A. Palano[ab], and M. Pappagallo[ab]
INFN Sezione di Bari[a]; Dipartmento di Fisica, Università di Bari[b], I-70126 Bari, Italy

G. Eigen, B. Stugu, and L. Sun
University of Bergen, Institute of Physics, N-5007 Bergen, Norway

G. S. Abrams, M. Battaglia, D. N. Brown, R. N. Cahn, R. G. Jacobsen, L. T. Kerth,
Yu. G. Kolomensky, G. Lynch, I. L. Osipenkov, M. T. Ronan,* K. Tackmann, and T. Tanabe
Lawrence Berkeley National Laboratory and University of California, Berkeley, California 94720, USA

C. M. Hawkes, N. Soni, and A. T. Watson
University of Birmingham, Birmingham, B15 2TT, United Kingdom

H. Koch and T. Schroeder
Ruhr Universität Bochum, Institut für Experimentalphysik 1, D-44780 Bochum, Germany

D. Walker
University of Bristol, Bristol BS8 1TL, United Kingdom

D. J. Asgeirsson, B. G. Fulsom, C. Hearty, T. S. Mattison, and J. A. McKenna
University of British Columbia, Vancouver, British Columbia, Canada V6T 1Z1

M. Barrett and A. Khan
Brunel University, Uxbridge, Middlesex UB8 3PH, United Kingdom

V. E. Blinov, A. D. Bukin, A. R. Buzykaev, V. P. Druzhinin, V. B. Golubev,
A. P. Onuchin, S. I. Serednyakov, Yu. I. Skovpen, E. P. Solodov, and K. Yu. Todyshev
Budker Institute of Nuclear Physics, Novosibirsk 630090, Russia

M. Bondioli, S. Curry, I. Eschrich, D. Kirkby, A. J. Lankford, P. Lund, M. Mandelkern, E. C. Martin, and D. P. Stoker
University of California at Irvine, Irvine, California 92697, USA

S. Abachi and C. Buchanan
University of California at Los Angeles, Los Angeles, California 90024, USA

H. Atmacan, J. W. Gary, F. Liu, O. Long, G. M. Vitug, Z. Yasin, and L. Zhang
University of California at Riverside, Riverside, California 92521, USA

V. Sharma
University of California at San Diego, La Jolla, California 92093, USA

C. Campagnari, T. M. Hong, D. Kovalskyi, M. A. Mazur, and J. D. Richman
University of California at Santa Barbara, Santa Barbara, California 93106, USA

T. W. Beck, A. M. Eisner, C. J. Flacco, C. A. Heusch, J. Kroseberg, W. S. Lockman,
A. J. Martinez, T. Schalk, B. A. Schumm, A. Seiden, M. G. Wilson, and L. O. Winstrom
University of California at Santa Cruz, Institute for Particle Physics, Santa Cruz, California 95064, USA

C. H. Cheng, D. A. Doll, B. Echenard, F. Fang, D. G. Hitlin, I. Narsky, T. Piatenko, and F. C. Porter
California Institute of Technology, Pasadena, California 91125, USA

R. Andreassen, G. Mancinelli, B. T. Meadows, K. Mishra, and M. D. Sokoloff
University of Cincinnati, Cincinnati, Ohio 45221, USA

P. C. Bloom, W. T. Ford, A. Gaz, J. F. Hirschauer, M. Nagel,
U. Nauenberg, J. G. Smith, K. A. Ulmer, and S. R. Wagner
University of Colorado, Boulder, Colorado 80309, USA

R. Ayad,[†] A. Soffer,[‡] W. H. Toki, and R. J. Wilson
Colorado State University, Fort Collins, Colorado 80523, USA

E. Feltresi, A. Hauke, H. Jasper, M. Karbach, J. Merkel, A. Petzold, B. Spaan, and K. Wacker
Technische Universität Dortmund, Fakultät Physik, D-44221 Dortmund, Germany

M. J. Kobel, R. Nogowski, K. R. Schubert, R. Schwierz, and A. Volk
Technische Universität Dresden, Institut für Kern- und Teilchenphysik, D-01062 Dresden, Germany

D. Bernard, G. R. Bonneaud, E. Latour, and M. Verderi
Laboratoire Leprince-Ringuet, CNRS/IN2P3, Ecole Polytechnique, F-91128 Palaiseau, France

P. J. Clark, S. Playfer, and J. E. Watson
University of Edinburgh, Edinburgh EH9 3JZ, United Kingdom

M. Andreotti[ab], D. Bettoni[a], C. Bozzi[a], R. Calabrese[ab], A. Cecchi[ab], G. Cibinetto[ab],
P. Franchini[ab], E. Luppi[ab], M. Negrini[ab], A. Petrella[ab], L. Piemontese[a], and V. Santoro[ab]
INFN Sezione di Ferrara[a]; Dipartimento di Fisica, Università di Ferrara[b], I-44100 Ferrara, Italy

R. Baldini-Ferroli, A. Calcaterra, R. de Sangro, G. Finocchiaro,
S. Pacetti, P. Patteri, I. M. Peruzzi,[§] M. Piccolo, M. Rama, and A. Zallo
INFN Laboratori Nazionali di Frascati, I-00044 Frascati, Italy

A. Buzzo[a], R. Contri[ab], M. Lo Vetere[ab], M. M. Macri[a], M. R. Monge[ab],
S. Passaggio[a], C. Patrignani[ab], E. Robutti[a], A. Santroni[ab], and S. Tosi[ab]
INFN Sezione di Genova[a]; Dipartimento di Fisica, Università di Genova[b], I-16146 Genova, Italy

K. S. Chaisanguanthum and M. Morii
Harvard University, Cambridge, Massachusetts 02138, USA

A. Adametz, J. Marks, S. Schenk, and U. Uwer
Universität Heidelberg, Physikalisches Institut, Philosophenweg 12, D-69120 Heidelberg, Germany

V. Klose and H. M. Lacker
Humboldt-Universität zu Berlin, Institut für Physik, Newtonstr. 15, D-12489 Berlin, Germany

D. J. Bard, P. D. Dauncey, J. A. Nash, and M. Tibbetts
Imperial College London, London, SW7 2AZ, United Kingdom

P. K. Behera, X. Chai, M. J. Charles, and U. Mallik
University of Iowa, Iowa City, Iowa 52242, USA

J. Cochran, H. B. Crawley, L. Dong, W. T. Meyer, S. Prell, E. I. Rosenberg, and A. E. Rubin
Iowa State University, Ames, Iowa 50011-3160, USA

Y. Y. Gao, A. V. Gritsan, Z. J. Guo, and C. K. Lae
Johns Hopkins University, Baltimore, Maryland 21218, USA

N. Arnaud, J. Béquilleux, A. D'Orazio, M. Davier, J. Firmino da Costa, G. Grosdidier, F. Le Diberder, V. Lepeltier, A. M. Lutz, S. Pruvot, P. Roudeau, M. H. Schune, J. Serrano, V. Sordini,¶ A. Stocchi, and G. Wormser
Laboratoire de l'Accélérateur Linéaire, IN2P3/CNRS et Université Paris-Sud 11, Centre Scientifique d'Orsay, B. P. 34, F-91898 Orsay Cedex, France

D. J. Lange and D. M. Wright
Lawrence Livermore National Laboratory, Livermore, California 94550, USA

I. Bingham, J. P. Burke, C. A. Chavez, J. R. Fry, E. Gabathuler, R. Gamet, D. E. Hutchcroft, D. J. Payne, and C. Touramanis
University of Liverpool, Liverpool L69 7ZE, United Kingdom

A. J. Bevan, C. K. Clarke, K. A. George, F. Di Lodovico, R. Sacco, and M. Sigamani
Queen Mary, University of London, London, E1 4NS, United Kingdom

G. Cowan, H. U. Flaecher, D. A. Hopkins, S. Paramesvaran, F. Salvatore, and A. C. Wren
University of London, Royal Holloway and Bedford New College, Egham, Surrey TW20 0EX, United Kingdom

D. N. Brown and C. L. Davis
University of Louisville, Louisville, Kentucky 40292, USA

A. G. Denig, M. Fritsch, and W. Gradl
Johannes Gutenberg-Universität Mainz, Institut für Kernphysik, D-55099 Mainz, Germany

K. E. Alwyn, D. Bailey, R. J. Barlow, Y. M. Chia, C. L. Edgar, G. Jackson, G. D. Lafferty, T. J. West, and J. I. Yi
University of Manchester, Manchester M13 9PL, United Kingdom

J. Anderson, C. Chen, A. Jawahery, D. A. Roberts, G. Simi, and J. M. Tuggle
University of Maryland, College Park, Maryland 20742, USA

C. Dallapiccola, X. Li, E. Salvati, and S. Saremi
University of Massachusetts, Amherst, Massachusetts 01003, USA

R. Cowan, D. Dujmic, P. H. Fisher, S. W. Henderson, G. Sciolla, M. Spitznagel, F. Taylor, R. K. Yamamoto, and M. Zhao
Massachusetts Institute of Technology, Laboratory for Nuclear Science, Cambridge, Massachusetts 02139, USA

P. M. Patel and S. H. Robertson
McGill University, Montréal, Québec, Canada H3A 2T8

A. Lazzaro[ab], V. Lombardo[a], and F. Palombo[ab]
INFN Sezione di Milano[a]; Dipartimento di Fisica, Università di Milano[b], I-20133 Milano, Italy

J. M. Bauer, L. Cremaldi, R. Godang,[**] R. Kroeger, D. A. Sanders, D. J. Summers, and H. W. Zhao
University of Mississippi, University, Mississippi 38677, USA

M. Simard, P. Taras, and F. B. Viaud
Université de Montréal, Physique des Particules, Montréal, Québec, Canada H3C 3J7

H. Nicholson
Mount Holyoke College, South Hadley, Massachusetts 01075, USA

G. De Nardo[ab], L. Lista[a], D. Monorchio[ab], G. Onorato[ab], and C. Sciacca[ab]
INFN Sezione di Napoli[a]; Dipartimento di Scienze Fisiche, Università di Napoli Federico II[b], I-80126 Napoli, Italy

G. Raven and H. L. Snoek
NIKHEF, National Institute for Nuclear Physics and High Energy Physics, NL-1009 DB Amsterdam, The Netherlands

C. P. Jessop, K. J. Knoepfel, J. M. LoSecco, and W. F. Wang
University of Notre Dame, Notre Dame, Indiana 46556, USA

G. Benelli, L. A. Corwin, K. Honscheid, H. Kagan, R. Kass, J. P. Morris,
A. M. Rahimi, J. J. Regensburger, S. J. Sekula, and Q. K. Wong
Ohio State University, Columbus, Ohio 43210, USA

N. L. Blount, J. Brau, R. Frey, O. Igonkina, J. A. Kolb, M. Lu,
R. Rahmat, N. B. Sinev, D. Strom, J. Strube, and E. Torrence
University of Oregon, Eugene, Oregon 97403, USA

G. Castelli[ab], N. Gagliardi[ab], M. Margoni[ab], M. Morandin[a],
M. Posocco[a], M. Rotondo[a], F. Simonetto[ab], R. Stroili[ab], and C. Voci[ab]
INFN Sezione di Padova[a]; Dipartimento di Fisica, Università di Padova[b], I-35131 Padova, Italy

P. del Amo Sanchez, E. Ben-Haim, H. Briand, G. Calderini, J. Chauveau, P. David,
L. Del Buono, O. Hamon, Ph. Leruste, J. Ocariz, A. Perez, J. Prendki, and S. Sitt
Laboratoire de Physique Nucléaire et de Hautes Energies,
IN2P3/CNRS, Université Pierre et Marie Curie-Paris6,
Université Denis Diderot-Paris7, F-75252 Paris, France

L. Gladney
University of Pennsylvania, Philadelphia, Pennsylvania 19104, USA

M. Biasini[ab], R. Covarelli[ab], and E. Manoni[ab]
INFN Sezione di Perugia[a]; Dipartimento di Fisica, Università di Perugia[b], I-06100 Perugia, Italy

C. Angelini[ab], G. Batignani[ab], S. Bettarini[ab], M. Carpinelli[ab],†† A. Cervelli[ab], F. Forti[ab], M. A. Giorgi[ab],
A. Lusiani[ac], G. Marchiori[ab], M. Morganti[ab], N. Neri[ab], E. Paoloni[ab], G. Rizzo[ab], and J. J. Walsh[a]
INFN Sezione di Pisa[a]; Dipartimento di Fisica, Università di Pisa[b]; Scuola Normale Superiore di Pisa[c], I-56127 Pisa, Italy

D. Lopes Pegna, C. Lu, J. Olsen, A. J. S. Smith, and A. V. Telnov
Princeton University, Princeton, New Jersey 08544, USA

F. Anulli[a], E. Baracchini[ab], G. Cavoto[a], D. del Re[ab], E. Di Marco[ab], R. Faccini[ab],
F. Ferrarotto[a], F. Ferroni[ab], M. Gaspero[ab], P. D. Jackson[a], L. Li Gioi[a],
M. A. Mazzoni[a], S. Morganti[a], G. Piredda[a], F. Polci[ab], F. Renga[ab], and C. Voena[a]
INFN Sezione di Roma[a]; Dipartimento di Fisica,
Università di Roma La Sapienza[b], I-00185 Roma, Italy

M. Ebert, T. Hartmann, H. Schröder, and R. Waldi
Universität Rostock, D-18051 Rostock, Germany

T. Adye, B. Franek, E. O. Olaiya, and F. F. Wilson
Rutherford Appleton Laboratory, Chilton, Didcot, Oxon, OX11 0QX, United Kingdom

S. Emery, M. Escalier, L. Esteve, S. F. Ganzhur, G. Hamel de Monchenault,
W. Kozanecki, G. Vasseur, Ch. Yèche, and M. Zito
CEA, Irfu, SPP, Centre de Saclay, F-91191 Gif-sur-Yvette, France

X. R. Chen, H. Liu, W. Park, M. V. Purohit, R. M. White, and J. R. Wilson
University of South Carolina, Columbia, South Carolina 29208, USA

M. T. Allen, D. Aston, R. Bartoldus, P. Bechtle, J. F. Benitez, R. Cenci, J. P. Coleman, M. R. Convery,
J. C. Dingfelder, J. Dorfan, G. P. Dubois-Felsmann, W. Dunwoodie, R. C. Field, A. M. Gabareen,

S. J. Gowdy, M. T. Graham, P. Grenier, C. Hast, W. R. Innes, J. Kaminski, M. H. Kelsey, H. Kim, P. Kim, M. L. Kocian, D. W. G. S. Leith, S. Li, B. Lindquist, S. Luitz, V. Luth, H. L. Lynch, D. B. MacFarlane, H. Marsiske, R. Messner, D. R. Muller, H. Neal, S. Nelson, C. P. O'Grady, I. Ofte, A. Perazzo, M. Perl, B. N. Ratcliff, A. Roodman, A. A. Salnikov, R. H. Schindler, J. Schwiening, A. Snyder, D. Su, M. K. Sullivan, K. Suzuki, S. K. Swain, J. M. Thompson, J. Va'vra, A. P. Wagner, M. Weaver, C. A. West, W. J. Wisniewski, M. Wittgen, D. H. Wright, H. W. Wulsin, A. K. Yarritu, K. Yi, C. C. Young, and V. Ziegler
Stanford Linear Accelerator Center, Stanford, California 94309, USA

P. R. Burchat, A. J. Edwards, S. A. Majewski, T. S. Miyashita, B. A. Petersen, and L. Wilden
Stanford University, Stanford, California 94305-4060, USA

S. Ahmed, M. S. Alam, J. A. Ernst, B. Pan, M. A. Saeed, and S. B. Zain
State University of New York, Albany, New York 12222, USA

S. M. Spanier and B. J. Wogsland
University of Tennessee, Knoxville, Tennessee 37996, USA

R. Eckmann, J. L. Ritchie, A. M. Ruland, C. J. Schilling, and R. F. Schwitters
University of Texas at Austin, Austin, Texas 78712, USA

B. W. Drummond, J. M. Izen, and X. C. Lou
University of Texas at Dallas, Richardson, Texas 75083, USA

F. Bianchi[ab], D. Gamba[ab], and M. Pelliccioni[ab]
INFN Sezione di Torino[a]; Dipartimento di Fisica Sperimentale, Università di Torino[b], I-10125 Torino, Italy

M. Bomben[ab], L. Bosisio[ab], C. Cartaro[ab], G. Della Ricca[ab], L. Lanceri[ab], and L. Vitale[ab]
INFN Sezione di Trieste[a]; Dipartimento di Fisica, Università di Trieste[b], I-34127 Trieste, Italy

V. Azzolini, N. Lopez-March, F. Martinez-Vidal, D. A. Milanes, and A. Oyanguren
IFIC, Universitat de Valencia-CSIC, E-46071 Valencia, Spain

J. Albert, Sw. Banerjee, B. Bhuyan, H. H. F. Choi, K. Hamano,
R. Kowalewski, M. J. Lewczuk, I. M. Nugent, J. M. Roney, and R. J. Sobie
University of Victoria, Victoria, British Columbia, Canada V8W 3P6

T. J. Gershon, P. F. Harrison, J. Ilic, T. E. Latham, and G. B. Mohanty
Department of Physics, University of Warwick, Coventry CV4 7AL, United Kingdom

H. R. Band, X. Chen, S. Dasu, K. T. Flood, Y. Pan, M. Pierini, R. Prepost, C. O. Vuosalo, and S. L. Wu
University of Wisconsin, Madison, Wisconsin 53706, USA

(Dated: November 5, 2008)

We report the results of a search for $Z(4430)^-$ decay to $J/\psi\pi^-$ or $\psi(2S)\pi^-$ in $B^{-,0} \to J/\psi\,\pi^- K^{0,+}$ and $B^{-,0} \to \psi(2S)\pi^- K^{0,+}$ decays. The data were collected with the *BABAR* detector at the SLAC PEP-II asymmetric-energy e^+e^- collider operating at center of mass energy 10.58 GeV, and the sample corresponds to an integrated luminosity of 413 fb^{-1}. Each $K\pi^-$ mass distribution exhibits clear $K^*(892)$ and $K_2^*(1430)$ signals, and the efficiency-corrected spectrum is well-described by a superposition of the associated Breit-Wigner intensity distributions, together with an S-wave contribution obtained from the LASS $I = 1/2$ $K\pi^-$ scattering amplitude measurements. Each $K\pi^-$ angular distribution varies significantly in structure with $K\pi^-$ mass, and is represented in terms of low-order Legendre polynomial moments. We find that each $J/\psi\pi^-$ or $\psi(2S)\pi^-$ mass distribution is well-described by the reflection of the measured $K\pi^-$ mass and angular distribution structures. We see no significant evidence for a $Z(4430)^-$ signal for any of the processes investigated, neither in the total $J/\psi\pi^-$ or $\psi(2S)\pi^-$ mass distribution, nor in the corresponding distributions for the regions of $K\pi^-$ mass for which observation of the $Z(4430)^-$ signal was reported. We obtain branching fraction upper limits $\mathcal{B}(B^- \to Z^-\bar{K}^0, Z^- \to J/\psi\pi^-) < 1.5 \times 10^{-5}$, $\mathcal{B}(B^0 \to Z^-K^+, Z^- \to J/\psi\pi^-) < 0.4 \times 10^{-5}$, $\mathcal{B}(B^- \to Z^-\bar{K}^0, Z^- \to \psi(2S)\pi^-) < 4.7 \times 10^{-5}$, and $\mathcal{B}(B^0 \to Z^-K^+, Z^- \to \psi(2S)\pi^-) < 3.1 \times 10^{-5}$ at 95% confidence level, where the $Z(4430)^-$ mass and width have been fixed to the reported central values.

PACS numbers: 12.39.Mk,12.40.Yx,13.25.Hw,14.40Gx

I. INTRODUCTION

In the original paper in which he proposed the Quark Model [1], Gell-Mann stated that "Baryons can now be constructed from quarks using the combinations (qqq), $(qqqq\bar{q})$, *etc.*, while mesons are made out of $(q\bar{q})$, $(qq\bar{q}\bar{q})$, *etc.*". He chose the lowest configurations to create the representations describing the known meson and baryon states. However, the higher configurations were not *a priori* excluded, and experimentalists and theorists have been seeking evidence supporting the existence of such states ever since.

In the baryon sector, resonant structure in the KN system would be indicative of five-quark content, and searches for states of this type have been carried out since the mid-1960's, mainly through partial-wave analysis of KN elastic and charge-exchange scattering data. In recent years, there has been a great deal of activity focused on the search for the conjectured $\Theta(1540)^+$ pentaquark state decaying to K^0p. However, the initial low-statistics signals claimed in a variety of experimental contexts have not withstood high-statistics scrutiny, and the existence of this state must be considered to be in doubt at the present time. The subject is reviewed in Ref. [2], and the status is updated in Ref. [3].

In the meson sector, attention has been focused over the years mainly on the $a_0(980)$ and the $f_0(980)$ scalar mesons as possible four-quark states. However, the discovery of the $D^*_{s0}(2317)$ and the $D_{s1}(2460)$, with their unexpectedly low mass values, and the observation of many new charmonium-like states above threshold for decay to open charm, have led to speculation that certain of these may be four-quark states (see *e.g.* Ref. [4]), although in no case has this been clearly established. In this regard, it follows that the recent paper from the Belle Collaboration [5] which reports the observation of a resonance-like structure, the $Z(4430)^-$, in the $\psi(2S)\pi^-$ system produced in the decays $B^{-,0} \to \psi(2S)\pi^-K^{0,+}$ [6] has generated a great deal of interest (see *e.g.* Ref. [7], and references therein). Such a state must have a minimum quark content $(c\bar{c}d\bar{u})$, and would represent the unequivocal manifestation of a four-quark meson state.

It is clearly important to seek confirmation of the Belle observation, not only in the $\psi(2S)\pi^-$ system, but also for the $J/\psi\pi^-$ combination, which might also show evidence of a $Z(4430)^-$ signal or of a similar lower mass state [8]. Consequently, in this paper we present a *BABAR* analysis of the entire Dalitz plot corresponding to the decays $B^{-,0} \to \psi(2S)\pi^-K^{0,+}$ and in parallel pursue an identical analysis of our $B^{-,0} \to J/\psi\pi^-K^{0,+}$ data. Both analyses make use of the complete *BABAR* data sample accrued at the $\Upsilon(4S)$ resonance. In this regard, we first seek a representation of the $K\pi^-$ mass and angular distribution structures, which dominate the final states under study, in terms of their expected low-angular-momentum intensity contributions. We then investigate the reflection of each $K\pi^-$ system into its associated $\psi\pi^-$ [9] mass distribution in order to establish the need for any additional narrow signal.

The *BABAR* detector and the data sample are described briefly in Sec. II, and the event selection procedures are discussed in Sec. III. In Sec. IV, the Dalitz plots and their uncorrected invariant mass projections are shown for the B meson signal regions. Since the analysis emphasizes this search for narrow structure in the $J/\psi\pi^-$ and $\psi(2S)\pi^-$ mass distributions, the mass resolution dependence on invariant mass for these systems is analyzed in Sec. V. Similarly, it is important to understand the behavior of the event reconstruction efficiency over each final state Dalitz plot and to correct for it before assessing the significance of any observed mass structures. The procedure followed is described in Appendix A, and the results are summarized in Sec. VI. Fits to the corrected $K\pi^-$ mass distributions are discussed in Sec. VII, and the $K\pi^-$ angular distribution structure as a function of $K\pi^-$ mass is represented in terms of Legendre polynomial moments as described in Sec. VIII. In Sec. IX, the reflections of the observed $K\pi^-$ mass and angular structures onto the $J/\psi\pi^-$ and $\psi(2S)\pi^-$ mass distributions are compared to the corresponding efficiency-corrected distributions, and in Sec. X our results are discussed in relation to those in the Belle publication. The *BABAR* $\psi\pi^-$ mass distributions are fitted in Sec. XI, and we present a summary and our conclusions in Sec. XII. Finally, acknowledgments are expressed in Sec. XIII.

II. THE *BABAR* DETECTOR AND DATA SAMPLE

The data used in this analysis were collected with the *BABAR* detector at the PEP-II asymmetric-energy e^+e^- collider operating at a center-of-mass (c.m.) energy of 10.58 GeV.

A detailed description of the *BABAR* detector can be found in Ref. [10]. Charged particle tracks are detected with a five-layer, double-sided silicon vertex tracker (SVT) and a 40-layer drift chamber (DCH), filled with a helium-isobutane gas mixture, and coaxial with the cryostat of a superconducting solenoidal magnet,

*Deceased
†Now at Temple University, Philadelphia, Pennsylvania 19122, USA
‡Now at Tel Aviv University, Tel Aviv, 69978, Israel
§Also with Università di Perugia, Dipartimento di Fisica, Perugia, Italy
¶Also with Università di Roma La Sapienza, I-00185 Roma, Italy
**Now at University of South Alabama, Mobile, Alabama 36688, USA
††Also with Università di Sassari, Sassari, Italy

which produces a magnetic field of approximately 1.5 T. The charged-particle momentum resolution is given by $(\delta P_T/P_T)^2 = (0.0013 P_T)^2 + (0.0045)^2$, where P_T is the transverse momentum measured in GeV/c. The SVT, with a typical coordinate resolution of 10 μm, measures the impact parameters of charged particle tracks in both the plane transverse to the beam direction and along the collision axis; it also supports stand-alone reconstruction of low-P_T charged particle tracks.

Charged particle types are identified from specific ionization energy loss (dE/dx) measured in the DCH and SVT, and from Cherenkov radiation detected in a ring-imaging Cherenkov device. Electrons are identified by means of a CsI(Tl) electromagnetic calorimeter (EMC).

The return yoke of the superconducting coil is instrumented with resistive plate chambers for the identification of muons and the detection of clusters produced by K_L and neutron interactions. For the latter part of the experiment these chambers were replaced by limited streamer tubes in the barrel region of the detector [11].

In this analysis, we use a data sample corresponding to an integrated luminosity of 413 fb^{-1}, which is equivalent to the production of approximately 455 million $B\bar{B}$ pairs.

III. EVENT SELECTION

We reconstruct events in four decay modes [6]:

$$B^- \rightarrow J/\psi \pi^- K_S^0 , \quad (1)$$
$$B^0 \rightarrow J/\psi \pi^- K^+ , \quad (2)$$
$$B^- \rightarrow \psi(2S) \pi^- K_S^0 , \quad (3)$$
$$B^0 \rightarrow \psi(2S) \pi^- K^+ . \quad (4)$$

The event selection criteria were established by optimizing signal-to-background ratio using Monte Carlo (MC) simulated signal events, $B^{-,0} \rightarrow \psi\pi^- K^{0,+}$, and background, $B\bar{B}$ and $e^+e^- \rightarrow q\bar{q}$ ($q = u, d, s, c$), events.

For the data sample, a J/ψ candidate is formed by geometrically constraining an identified e^+e^- or $\mu^+\mu^-$ pair of tracks to a common vertex point and requiring a fit probability > 0.001. For $\mu^+\mu^-$, the invariant mass of the pair must in addition satisfy $3.06 < m_{\mu^+\mu^-} < 3.14$ GeV/c^2, while for e^+e^- the requirement is $2.95 < m_{e^+e^-} < 3.14$ GeV/c^2. In the latter case, the mass interval extends to lower values in order to allow for electron bremsstrahlung energy loss; if an electron-associated photon cluster of this type is found in the EMC, its four-momentum vector is included in the calculation of $m_{e^+e^-}$. The surviving J/ψ candidates were fitted to impose a constraint to the nominal mass value [3].

For $\psi(2S)$ decay to $\mu^+\mu^-$ or e^+e^- the same selection procedures are followed, but with invariant mass requirements $3.640 < m_{\mu^+\mu^-} < 3.740$ GeV/c^2 or $3.440 < m_{e^+e^-} < 3.740$ GeV/c^2. For $\psi(2S)$ decay to $J/\psi\pi^+\pi^-$, the J/ψ candidate is selected as previously described, and is fit again to incorporate a constraint to its nominal mass value [3]. This J/ψ and an identified $\pi^+\pi^-$ pair are geometrically constrained to a common vertex (fit probability > 0.001), and required to have an invariant mass in the range $3.655 < m_{J/\psi\pi^+\pi^-} < 3.715$ GeV/c^2. In the same manner as for the J/ψ, surviving candidates were then constrained to the nominal $\psi(2S)$ mass value [3].

A K_S^0 candidate is formed by geometrically constraining a pair of oppositely charged tracks to a common vertex (fit probability > 0.001); the tracks are treated as pions, but without particle-identification requirements, and the invariant mass of the pair must satisfy $0.472 < m_{\pi^+\pi^-} < 0.522$ GeV/c^2. A charged kaon candidate from the B meson decay must be identified as a kaon, but no particle identification is required of corresponding charged pion candidates.

The ψ, K and π candidates forming a B meson decay candidate are geometrically constrained to a common vertex, with fit probability > 0.001 required. For decay modes involving a K_S^0, the K_S^0 flight length with respect to this vertex must have $> +3$ standard deviation significance in order to reduce combinatoric background. The K_S^0 candidate is not mass constrained, since this was found to have a negligible effect on resolution.

We further define B meson decay candidates using the energy difference $\Delta E = E_B^* - \sqrt{s}/2$ in the center of mass (c.m.) frame, and the beam-energy substituted mass $m_{\rm ES} = \sqrt{((s/2 + \vec{p}_i \cdot \vec{p}_B)/E_i)^2 - \vec{p}_B^{\,2}}$, where $(E_i, \vec{p}_i)$ is the initial state four-momentum vector in the laboratory frame and $\sqrt{s}$ is the c.m. energy; E_B^* is the B meson energy in the c.m. and $\vec{p}_B$ is its laboratory frame momentum.

We require that B decay signal events satisfy $5.272 < m_{\rm ES} < 5.286$ GeV/c^2 and $|\Delta E| < 0.020$ GeV. In order to correct for background events in the signal region, we define a ΔE sideband region by $0.030 < |\Delta E| < 0.050$ GeV; we have verified through MC studies that sideband events in the $m_{\rm ES}$ signal range correctly represent background in the B meson signal region. We refer to the procedure by which we correct for background in the signal region by subtracting the ΔE sideband events in the $m_{\rm ES}$ signal range by the term "sideband subtraction".

In Figs. 1(a)-(d) we show the $m_{\rm ES}$ distributions in the ΔE signal region for the decay processes of Eqs. (1)- (4), where the filled histograms show the sideband distributions. We fit each distribution with a signal Gaussian function with mass and width as free parameters, and an ARGUS background function [12] with a free exponential slope parameter. In each figure, the solid curve represents the total function and the dashed curve shows the background contribution. Clear $m_{\rm ES}$ signals are observed in Figs. 1(a)-(d), and in each figure the sideband distribution is consistent with the fitted background.

The ΔE distributions for the $m_{\rm ES}$ signal region (Figs. 1(e)-(h)) exhibit clear signal peaks. We fit each distribution with a linear background function and a signal function consisting of two Gaussian functions with a common center; all parameters are free in the fits. In each case, the filled histogram is from the $m_{\rm ES}$ sideband region defined by $5.250 < m_{ES} < 5.264$ GeV/c^2, and is

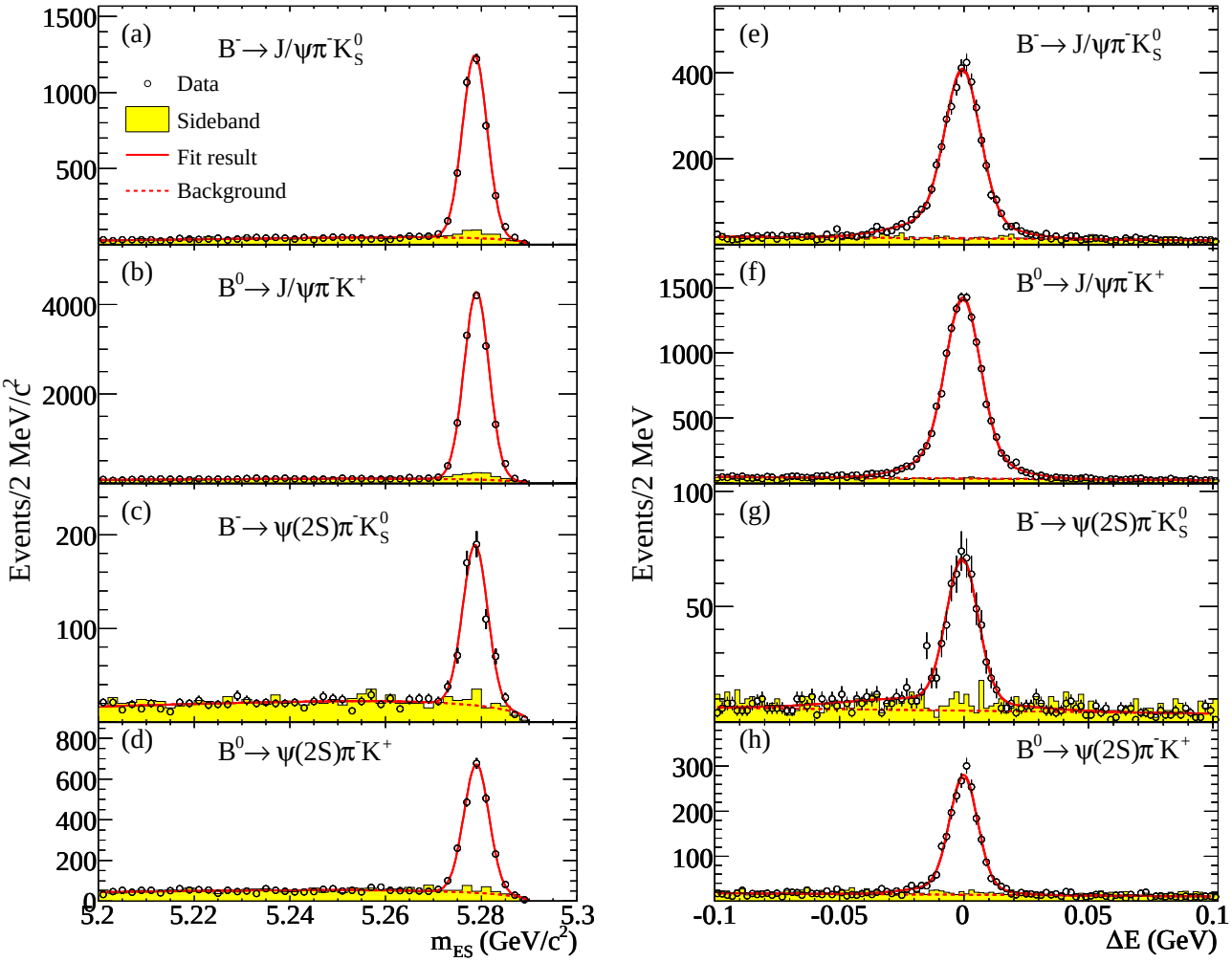

FIG. 1: The $m_{\rm ES}$ distributions, (a)-(d), and (ΔE) distributions, (e)-(h), for the decay modes $B^- \to J/\psi\pi^- K^0_S$, $B^0 \to J/\psi\pi^- K^+$, $B^- \to \psi(2S)\pi^- K^0_S$, and $B^0 \to \psi(2S)\pi^- K^+$. The points show the data, and the solid curves represent the fit functions. The dashed curves indicate the background contributions, and the filled histograms show the corresponding distributions for the sideband regions.

in good agreement with the fitted background. For the decay modes of Eqs. (1)-(4), the fraction of events with more than one B meson signal candidate ranges from 0.5 to 1.1 %. For such events, the candidate with the smallest value of $|\Delta E|$ is selected.

We summarize the principal selection criteria in Table I, and in Table II provide an overview of the data samples in the B-meson signal region used in the analysis described in this paper.

IV. THE DALITZ PLOTS AND INVARIANT MASS PROJECTIONS

The Dalitz plots of $m^2_{\psi\pi^-}$ versus $m^2_{K\pi^-}$ are shown in Fig. 2 for the signal regions defined in Table I for the B meson decay modes specified in Eqs. (1)-(4). The corresponding $m_{K\pi^-}$, $m_{\psi\pi^-}$, and $m_{\psi K}$ mass projections are represented by the data points in Figs. 3, 4, and 5, respectively. In each figure the filled histogram is obtained from the relevant ΔE sideband region.

In Fig. 3, the contributions due to the $K^*(892)$ dominate the mass distributions. Small, but clear, $K^*_2(1430)$ signals are evident for the J/ψ decay modes, and these seem to be present for the $\psi(2S)$ modes also. Previous analyses [13, 14] have shown that, for the J/ψ modes, the region between the $K^*(892)$ and $K^*_2(1430)$ signals ($\sim 1.1-1.3$ GeV/c^2) contains a significant $K\pi^-$ S-wave contribution. In the $K^*(892)$ region, the presence of the S-wave amplitude has been demonstrated through its interference with the $K^*(892)$ P-wave amplitude [14]. This interference yields a strong forward-backward asymmetry in the $K\pi^-$ angular distribution, as is seen in the vertical $K^*(892)$ bands of Fig. 2(b) and Fig. 2(d), and as is shown in Sec. VII, Figs. 13(a) and Fig. 13(c). These features of the $K\pi^-$ mass and angular distributions will be

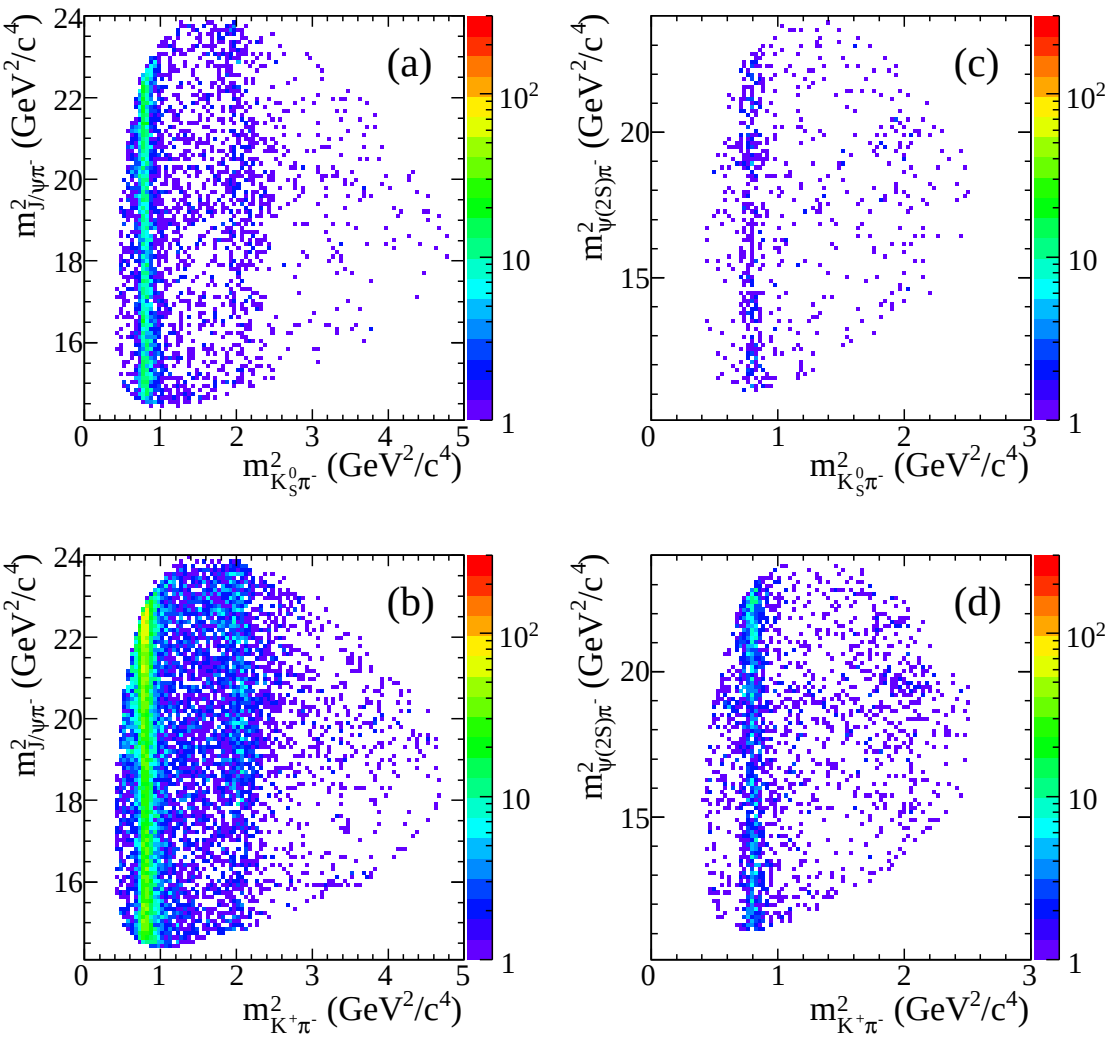

FIG. 2: The $m^2_{\psi\pi^-}$ versus $m^2_{K\pi^-}$ Dalitz plot distributions for the signal regions for the decay modes (a) $B^- \to J/\psi\pi^- K^0_S$, (b) $B^0 \to J/\psi\pi^- K^+$, (c) $B^- \to \psi(2S)\pi^- K^0_S$, (d) $B^0 \to \psi(2S)\pi^- K^+$. The intensity scale is logarithmic.

analyzed in detail in Secs. VII and VIII below.

The $m_{\psi\pi^-}$ distributions of Fig. 4 show no peaking structure at the mass reported for the $Z(4430)^-$ [5] (indicated by the dashed vertical line in each figure). In Fig. 4(b) there seems to be a peak at ~ 4.65 GeV/c^2 and perhaps a weaker one just below 4.4 GeV/c^2, while in Figs. 4(c) and (d) there seems to be a peak just below ~ 4.5 GeV/c^2. These features are discussed in Secs. X and XI in conjunction with reflections resulting from the $K\pi^-$ mass and angular structures.

Similarly, the $m_{\psi K}$ distributions of Fig. 5 show no evidence of narrow structure. In fact, in overall shape these distributions approximate mirror images of those in Fig. 4. This is not unexpected if both result primarily from $K\pi^-$ reflection, since then the high-mass region of one distribution would be correlated strongly with the low mass region of the other, and *vice versa*. Since Fig. 5 shows no evidence of interesting features, and since our emphasis in this paper is on the search for the $Z(4430)^-$, we do not discuss the ψK systems any further in the present analysis.

We note that in Figs. 3-5, and in other invariant mass distributions to follow, the J/ψ-$\psi(2S)$ mass difference causes significant differences in the range spanned in the respective decay modes. This should be kept in mind when making J/ψ-$\psi(2S)$ comparisons.

V. THE $\psi\pi^-$ MASS RESOLUTION

In Ref. [5], the width of the $Z(4430)^-$ is given as 45^{+35}_{-18} MeV, where we have combined statistical and systematic errors in quadrature. This value is very similar to that of the $K^*(892)$ [3], although with larger uncertain-

TABLE I: Summary of the principal criteria used to select B candidates.

Selection category	criterion
$J/\psi \to e^+e^-$	$2.95 < m_{ee} < 3.14$ GeV/c^2
$J/\psi \to \mu^+\mu^-$	$3.06 < m_{\mu\mu} < 3.14$ GeV/c^2
$\psi(2S) \to e^+e^-$	$3.44 < m_{ee} < 3.74$ GeV/c^2
$\psi(2S) \to J/\psi\pi^+\pi^-$ ($J/\psi \to e^+e^-$)	$3.655 < m_{J/\psi\pi\pi} < 3.715$ GeV/c^2
$\psi(2S) \to \mu^+\mu^-$	$3.64 < m_{\mu\mu} < 3.74$ GeV/c^2
$\psi(2S) \to J/\psi\pi^+\pi^-$ ($J/\psi \to \mu^+\mu^-$)	$3.655 < m_{J/\psi\pi\pi} < 3.715$ GeV/c^2
$K^0_S \to \pi^+\pi^-$	$0.472 < m_{\pi\pi} < 0.522$ GeV/c^2
Flight length significance	$> +3\sigma$
$m_{\rm ES}$ signal region	$5.272 < m_{\rm ES} < 5.286$ GeV/c^2
ΔE signal region	$\lvert\Delta E\rvert < 0.020$ GeV

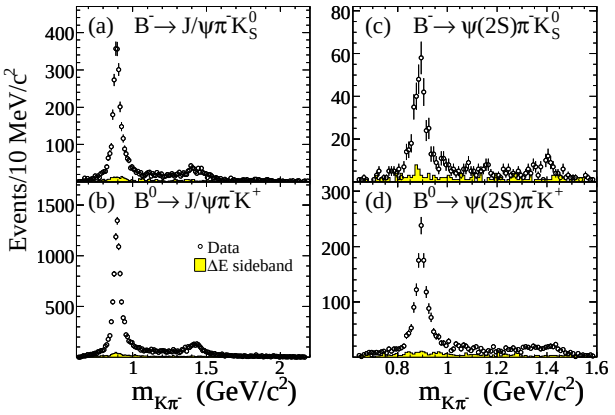

FIG. 3: The $m_{K\pi^-}$ mass projections for the Dalitz plots of Fig. 2. The data points are for the $m_{\rm ES}$-ΔE signal regions, and the filled histograms are for the ΔE sideband regions.

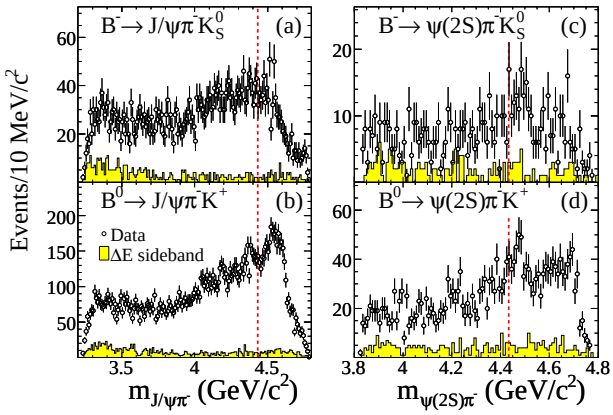

FIG. 4: The $m_{\psi\pi^-}$ mass projections for the Dalitz plots of Fig. 2. The data points are for the $m_{\rm ES}$-ΔE signal regions, and the filled histograms are for the ΔE sideband regions. The dashed vertical lines indicate $m_{\psi\pi^-} = 4.433$ GeV/c^2.

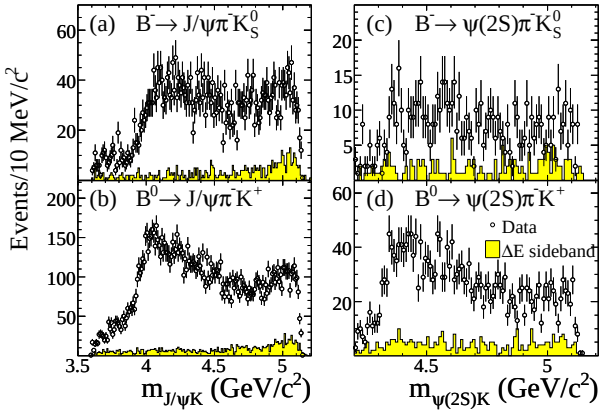

FIG. 5: The $m_{\psi K}$ mass projections for the Dalitz plots of Fig. 2. The data points are for the $m_{\rm ES}$-ΔE signal regions, and the filled histograms are for the ΔE sideband regions.

ties, which we have no difficulty observing, as shown in Fig. 3. However, mass resolution degrades with increasing Q-value, where Q-value is the difference between the invariant mass value in question and the corresponding threshold mass value. Since the Q-value for the $K^*(892)$ is only $\sim$ 260 MeV/c^2, while that for the $Z(4430)^-$ is $\sim$ 600 MeV/c^2 in the $\psi(2S)\pi$ mode, and would be $\sim$ 1200 MeV/c^2 in the $J/\psi\pi$ mode, the mass resolution should be worse for the $Z(4430)^-$ than for the $K^*(892)$, and hence should be systematically investigated.

We do this by using MC simulated data for the B meson decay modes of Eqs. (1)-(4). For each mode, the reconstructed events were divided into 50 MeV/c^2 intervals of $\psi\pi^-$ mass, and within each interval it was found

TABLE II: The data samples used in the analysis.

Decay mode	Signal region events	ΔE sideband events	Net analysis sample
$B^- \to J/\psi\pi^- K_S^0$	4229 ± 65	485 ± 22	3744 ± 68
$B^0 \to J/\psi\pi^- K^+$	14251 ± 119	1269 ± 36	12982 ± 124
$B^- \to \psi(2S)\pi^- K_S^0$	703 ± 26	161 ± 13	542 ± 29
$B^0 \to \psi(2S)\pi^- K^+$	2405 ± 49	384 ± 20	2021 ± 53

that the distribution of (reconstructed - generated) $\psi\pi^-$ mass could be described by a double Gaussian function with a common mean at zero. The local $\psi\pi^-$ mass resolution is characterized by the half-width-at-half-maximum (HWHM) value for this line shape, and the dependence of this quantity on $\psi\pi^-$ mass is shown in Fig. 6 for the individual decay modes. For both J/ψ modes, the resolution varies from ~ 2 MeV/c^2 at threshold to ~ 9 MeV/c^2 at the maximum mass value, while for both $\psi(2S)\pi$ modes, the variation is from $\sim 2-6$ MeV/c^2. At the $Z(4430)^-$ mass value, indicated by the dashed vertical lines in Fig. 6, the resolution is ~ 4 MeV/c^2 for $\psi(2S)\pi$, and ~ 7 MeV/c^2 for $J/\psi\pi$. We note that, for $J/\psi\pi$, the resolution at a Q-value of ~ 600 MeV/c^2 is essentially the same as for $\psi(2S)\pi$ at the $Z(4430)^-$. It follows that failure to observe the $Z(4430)^-$ in its $J/\psi\pi^-$ or $\psi(2S)\pi^-$ decay mode in the present experiment should not be attributed to inadequate mass resolution.

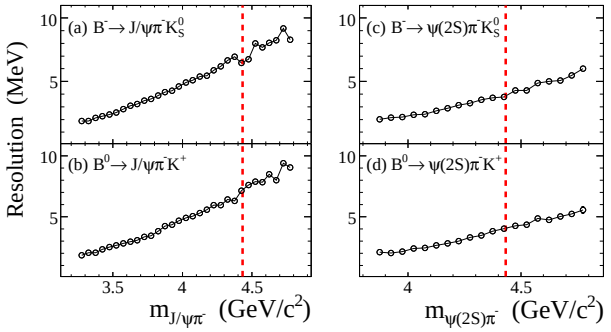

FIG. 6: The $\psi\pi^-$ mass resolution in 50 MeV/c^2 intervals as a function of $\psi\pi^-$ mass for the decay modes (a) $B^- \to J/\psi\pi^- K_S^0$, (b) $B^0 \to J/\psi\pi^- K^+$, (c) $B^- \to \psi(2S)\pi^- K_S^0$, and (d) $B^0 \to \psi(2S)\pi^- K^+$. The dashed vertical lines indicate $m_{\psi\pi^-} = 4.433$ GeV/c^2.

VI. EFFICIENCY CORRECTION

In the search for the $Z(4430)^-$, a detailed understanding of event reconstruction efficiency over the entire final state Dalitz plot for each of the B meson decay processes of Eqs. (1)-(4) is necessary. This is because efficiency variation can, in principle, lead to the creation of spurious signals or to the distortion of real effects such that their significance is reduced. Even when the process of efficiency correction leads to no significant change in the interpretation of the data, it is important to demonstrate clearly that this is in fact the case.

The efficiency correction procedure which we follow is described in detail in Appendix A. For reasons discussed there, we use a "rectangular Dalitz plot" for which the variables are chosen to be $m_{K\pi^-}$ and $\cos\theta_K$, the normalized dot-product between the $K\pi^-$ three-momentum vector in the parent-B rest frame and the kaon three-momentum vector after a Lorentz transformation from the B rest frame to the $K\pi^-$ rest frame. For the Dalitz plots shown in Fig. 2, the y-axis variable, $m^2_{\psi\pi^-}$, varies linearly with $\cos\theta_K$.

The average efficiency E_0 depends on ψ decay mode, as shown in Fig. 7. The individual fitted curves in this figure are used to calculate the value of E_0 for an event at a particular value of $m_{K\pi^-}$ which has been reconstructed in the relevant ψ decay mode.

As explained in Appendix A, E_0 is then modulated by a linear combination of 12 Legendre polynomials in $\cos\theta_K$, whose multiplicative coefficients $E_1 - E_{12}$ are obtained from curves representing their individual $m_{K\pi^-}$ dependence. In this way, an efficiency value can be calculated for each reconstructed event in our data sample. The inverse of this efficiency then provides a weight-factor which is associated with this event in any distribution to which it contributes. This enables us to correct any distribution under study for efficiency-loss effects.

A specific example is provided by the $K\pi^-$ mass distributions of Fig. 8. A weight value for each event is calculated according to its particular ψ decay mode, as described above. The histograms of Fig. 8 are then formed

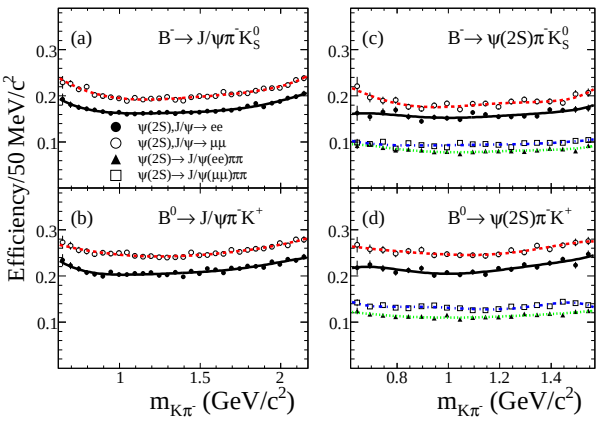

FIG. 7: The $m_{K\pi^-}$ dependence of the average efficiency, E_0, for the B meson decay processes (a) $B^- \to J/\psi\pi^- K_S^0$, (b) $B^0 \to J/\psi\pi^- K^+$, (c) $B^- \to \psi(2S)\pi^- K_S^0$, and (d) $B^0 \to \psi(2S)\pi^- K^+$. The key in (a) applies to all four figures, and, as indicated, the individual J/ψ and $\psi(2S)$ decay modes are treated separately. The curves result from fifth-order polynomial fits to the data points.

by summing these weights in each mass interval of each plot. Sideband subtraction is accomplished by assigning sideband events negative weight. The contributions from the different ψ decay modes are distinguished by shading, and the final histograms represent the sum of these contributions.

In Appendix A it is pointed out that the use of high-order Legendre polynomials is necessary because of significant decrease in efficiency for $\cos\theta_K \sim +1$ and $0.72 < m_{K\pi^-} < 0.92$ GeV/c^2, and for $\cos\theta_K \sim -1$ and $0.97 < m_{K\pi^-} < 1.27$ GeV/c^2. The former loss is due to the failure to reconstruct low-momentum pions in the laboratory frame, and the latter is due to a similar failure to reconstruct low-momentum kaons. The dependence of efficiency on laboratory frame momentum is shown in Fig. 9. In Figs. 9(a)-(d), there is a significant decrease in efficiency for pions of momentum < 0.1 GeV/c, while in Figs. 9(f),(h) there is similar decrease for charged kaons below ~ 0.25 GeV/c. For K_S^0, the effect is similar to that for charged pions (Figs. 9(e),(g)).

The Lorentz boost from the laboratory frame to the $K\pi^-$ rest frame translates the laboratory frame losses into the losses localized in $m_{K\pi^-}$ and $\cos\theta_K$ which our efficiency study reveals. The effect of these regions of low efficiency on the uncorrected $\psi\pi$ mass distributions is discussed in Sec. IX.

VII. FITS TO THE $K\pi^-$ MASS DISTRIBUTIONS

The most striking aspects of the Dalitz plots of Fig. 2 pertain to the $K\pi^-$ system, as shown explicitly in Fig. 3. In order to investigate the features of the $\psi\pi^-$ distributions of Fig. 4, it is necessary to understand how structure in the $K\pi^-$ mass and $\cos\theta_K$ distributions reflects into the $\psi\pi^-$ system. We begin this process by making detailed fits to the sideband-subtracted and efficiency-corrected $K\pi^-$ mass distributions of Fig. 8.

As discussed in Sec. IV, we expect that the $K\pi^-$ system can be described in terms of a superposition of S-, P-, and D-wave amplitudes. Since we correct for $\cos\theta_K$ dependence of the efficiency, it follows that the corrected $K\pi^-$ mass distributions of Fig. 8 can be described by a sum of S-, P-, and D-wave intensity contributions, since any interference terms vanish when integrated over $\cos\theta_K$. Consequently, we describe the $m_{K\pi^-}$ mass projections as follows,

$$\frac{dN}{dm_{K\pi}} = N\times \left[f_S\left(\frac{G_S}{\int G_S dm_{K\pi}}\right) + f_P\left(\frac{G_P}{\int G_P dm_{K\pi}}\right) + f_D\left(\frac{G_D}{\int G_D dm_{K\pi}}\right)\right], \quad (5)$$

where the integrals are over the full $m_{K\pi}$ range and the fractions f are such that

$$f_S + f_P + f_D = 1\,. \quad (6)$$

The P- and D-wave intensities, G_P and G_D, are expressed in terms of the squared moduli of Breit-Wigner (BW) amplitudes. For the P-wave,

$$G_P(m_{K\pi}) = \frac{B_P(m_{K\pi})(p\cdot q)\frac{q^2}{D_P(qR_P)}}{(m_P^2 - m_{K\pi}^2)^2 + m_P^2\Gamma_P^2(q,R_P)}\,, \quad (7)$$

where

- $B_P(m_{K\pi})$ describes the B-decay vertex;
- p is the momentum of the ψ in the B rest frame;
- q is the momentum of the K in the $K\pi^-$ rest frame;
- D_P is the P-wave Blatt-Weisskopf barrier factor with radius R_P [15];
- the mass-dependent total width is

$$\Gamma_P = \Gamma_P^0\left(\frac{q^2}{q_P^2}\right)\frac{D_P(q_P R_P)}{D_P(qR_P)}\left(\frac{q}{q_P}\right)\left(\frac{m_P}{m_{K\pi}}\right), \quad (8)$$

with $q_P = q$ evaluated at m_P; m_P is the mass, and Γ_P^0 the width, of the $K^*(892)$. We leave the mass and width free in the fits and choose $R_P = 3.0$ GeV^{-1} [18].

Similarly, for the D-wave,

$$G_D(m_{K\pi}) = \frac{B_D(m_{K\pi})(p\cdot q)\frac{q^4}{D_D(qR_D)}}{(m_D^2 - m_{K\pi}^2)^2 + m_D^2\Gamma_D^2(q,R_D)}\,, \quad (9)$$

where

- $B_D(m_{K\pi})$ describes the B-decay vertex;

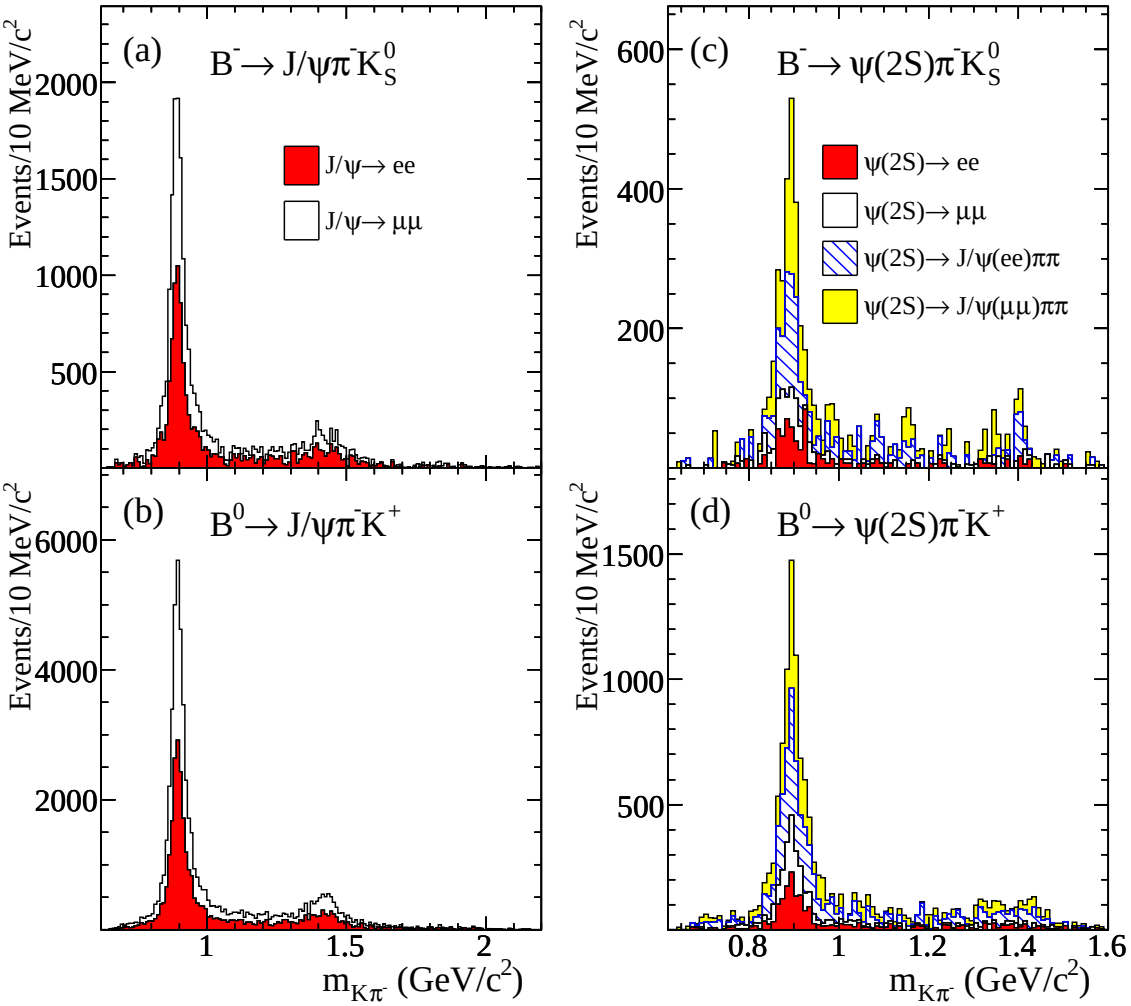

FIG. 8: The $K\pi^-$ mass distributions, after sideband subtraction and efficiency correction, for the decay modes (a) $B^- \to J/\psi\pi^- K_S^0$, (b) $B^0 \to J/\psi\pi^- K^+$, (c) $B^- \to \psi(2S)\pi^- K_S^0$, and (d) $B^0 \to \psi(2S)\pi^- K^+$. The contributions from the individual ψ decay modes are obtained separately, as described in the text, and are accumulated as indicated by the keys in (a) and (c), to form the final histograms.

- D_D is the D-wave Blatt-Weisskopf barrier factor with radius R_D [15];
- the mass-dependence of the total width is approximated by the $K\pi^-$ contribution as follows,

$$\Gamma_D = \Gamma_D^0 \left(\frac{q^4}{q_D^4}\right) \frac{D_D(q_D R_D)}{D_D(q R_D)} \left(\frac{q}{q_D}\right) \left(\frac{m_D}{m_{K\pi}}\right) , \quad (10)$$

with $q_D = q$ evaluated at m_D; m_D is the mass, and Γ_D^0 the width of the $K_2^*(1430)$. We fix m_D and Γ_D^0 to their nominal values [3] and choose $R_D = 1.5$ GeV^{-1} [16].

The S-wave contribution is described using the $I = 1/2$ amplitude for S-wave $K^-\pi^+$ elastic scattering [18]. We write

$$G_S(m_{K\pi}) = B_S(m_{K\pi})(p \cdot q)|T_S|^2 , \quad (11)$$

where $B_S(m_{K\pi})$ describes the B-decay vertex; T_S is the invariant amplitude, which is related to A_S, the complex $K\pi^-$ scattering amplitude, by

$$|T_S| = \left(\frac{m_{K\pi}}{q}\right) |A_S| . \quad (12)$$

For $m_{K\pi^-} > 1.5$ GeV/c^2, $|A_S|$ is obtained by interpolation from the measured values [16]. For lower mass values, A_S is a pure-elastic amplitude (within error) and

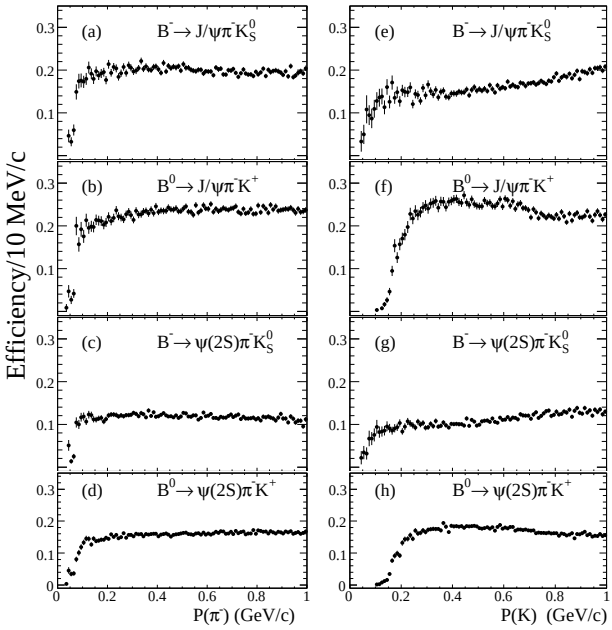

FIG. 9: (a)-(d): The dependence of efficiency on pion momentum in the laboratory frame for the B meson decay modes of Eqs. (1)-(4). (e)-(h): The corresponding efficiency dependence on kaon laboratory frame momentum.

is parameterized as

$$A_S = \frac{1}{\cot\delta_B - i} + e^{2i\delta_B}\left(\frac{1}{\cot\delta_R - i}\right), \qquad (13)$$

where the first term is non-resonant, and the second is a resonant term rotated by $2\delta_B$ in order to maintain elastic unitarity. In Eq. 13,

$$q\cot\delta_B = \frac{1}{a} + \frac{1}{2}rq^2\,, \qquad (14)$$

with $a = 1.94$ GeV^{-1} and $r = 1.76$ GeV^{-1} [16];

$$\cot\delta_R = \frac{m_S^2 - m_{K\pi}^2}{m_S\Gamma_S}\,, \qquad (15)$$

with

$$\Gamma_S = \Gamma_S^0\left(\frac{q}{q_S}\right)\frac{m_S}{m_{K\pi}}\,; \qquad (16)$$

m_S ($= 1.435$ GeV/c^2) is the mass of the $K_0^*(1430)$ resonance and Γ_S^0 ($= 0.279$ GeV) is its width [16]. We choose to fix the S-wave parameters to the indicated values.

Although the vertex functions B_S, B_P, and B_D depend, in principle, on $m_{K\pi}$, we find that our best fits to the mass distributions are obtained when each vertex function is set to one ($B_S = B_P = B_D = 1$). In this regard, we emphasize that our goal is not to obtain a precise amplitude decomposition of the $K\pi^-$ mass spectrum. This would require taking account of the angular correlations between the ψ decay products and the $K\pi^-$ system. For $K\pi^-$ S-, P-, and D-wave this is extremely complicated [17], and is far beyond the scope of the present analysis. Our aim is to obtain an accurate description of the $K\pi^-$ mass distributions in terms of the expected angular momentum contributions so that we can reliably project the observed structures onto the related $\psi\pi^-$ mass distributions.

The results of the fits to the $m_{K\pi^-}$ distributions of Fig. 8 are shown by the curves in Fig. 10. Good descriptions are obtained, even though each fit has only five free parameters and the fit function has exactly the same structure in each case.

Table III summarizes the output from the fits. The χ^2/NDF (NDF = Number of Degrees of Freedom) values are satisfactory, and the mass and width values for the $K^*(892)^0$ and $K^*(892)^-$ modes are internally consistent and agree with their nominal values [3]; the width values for the $\psi(2S)$ modes are slightly low, but the uncertainties are quite large because of the smaller data sample involved.

The fractional contributions for the two J/ψ modes agree well with each other, and there is similar agreement for the $\psi(2S)$ modes. This demonstrates that the charged and neutral $K\pi^-$ distributions are very similar in shape, and so we combine them for the remainder of the analysis, unless we explicitly indicate otherwise.

The results of repeating the fits for the combined distributions are shown in Fig. 11, where we use a logarithmic y-axis scale in order to display the individual contributions more clearly. The solid curves describe the distributions very well. For $m_{K\pi} \sim 0.7$ GeV/c^2, the curves in both plots are slightly below the data, and we believe that this results from the parameterization of the S-wave amplitude at low $K\pi^-$ mass values. If we normalize the S-wave amplitudes of Ref. [16] and Ref. [18] at 1.2 GeV/c^2 and average them from threshold to 1.2 GeV/c^2, the discrepancy is removed. However, the fits become slightly worse in the region between the two K^*'s. Since the latter region is very important to the present analysis, while the region around 0.7 GeV/c^2 is much less so, we do not make use of the modified S-wave amplitude.

Based on Table III, the following branching fractions can be calculated:

$$\mathcal{B}(B^- \to J/\psi\pi^-\bar{K}^0) = (1.101 \pm 0.021)\times 10^{-3}\,, \qquad (17)$$

$$\mathcal{B}(B^0 \to J/\psi\pi^-K^+) = (1.079 \pm 0.011)\times 10^{-3}\,, \qquad (18)$$

$$\mathcal{B}(B^- \to \psi(2S)\pi^-\bar{K}^0) = (0.588 \pm 0.034)\times 10^{-3}\,, \qquad (19)$$

$$\mathcal{B}(B^0 \to \psi(2S)\pi^-K^+) = (0.557 \pm 0.016)\times 10^{-3}\,, \qquad (20)$$

where we have corrected for the relevant J/ψ, $\psi(2S)$, $K_S^0 \to \pi^0\pi^0$, and K_L^0 branching fractions [3]. The quoted errors result from the statistical uncertainties of Table III. The published value corresponding to Eq. (18)

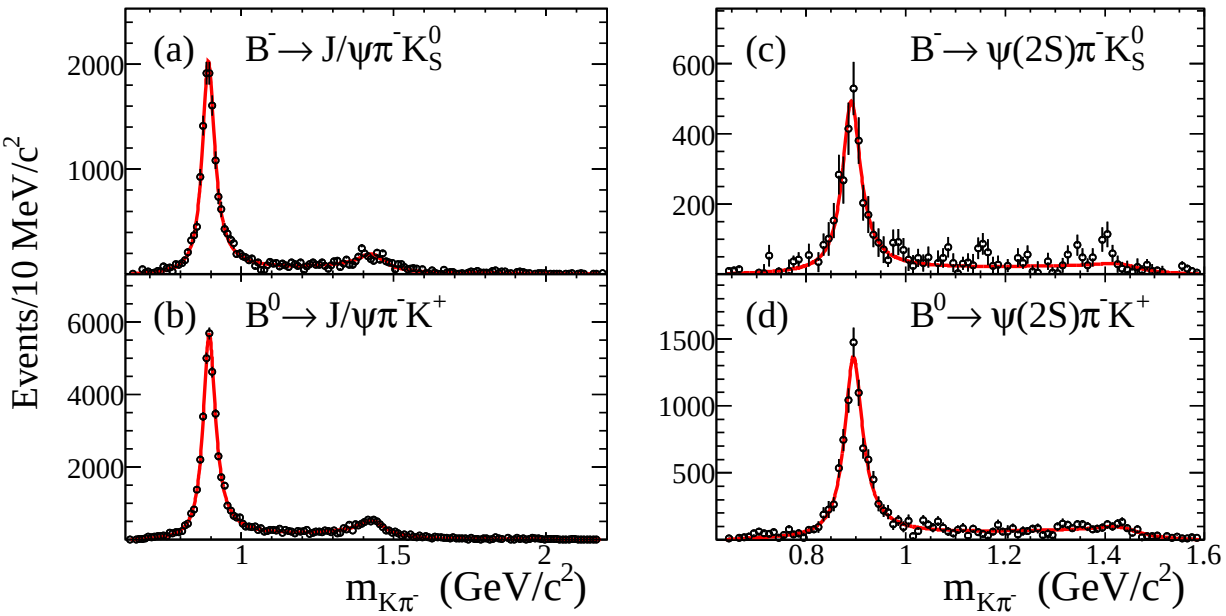

FIG. 10: The efficiency-corrected and sideband-subtracted $K\pi^-$ mass distributions of Fig. 8 for the decay modes (a) $B^- \to J/\psi\pi^- K^0_S$, (b) $B^0 \to J/\psi\pi^- K^+$, (c) $B^- \to \psi(2S)\pi^- K^0_S$, and (d) $B^0 \to \psi(2S)\pi^- K^+$. The data are shown as open dots, and the curves correspond to the fits described in the text.

TABLE III: Summary of the fit results corresponding to Fig. 10. For each decay mode, we list the total number of $K\pi$ events after efficiency-correction and sideband-subtraction, χ^2/NDF, $K^*(892)$ mass and width, and the percentage S-, P-, and D-wave intensity contributions. Only statistical uncertainties are given.

Mode	Corrected Events	χ^2/NDF	$m(K^*(892))$ (MeV/c^2)	$\Gamma(K^*(892))$ (MeV)	S-wave (%)	P-wave (%)	D-wave (%)
$B^- \to J/\psi\pi^- K^0_S$	20985±393	117.6/149	892.9±0.8	49.0±1.9	17.0±1.6	72.5±1.3	10.5±1.0
$B^0 \to J/\psi\pi^- K^+$	57231±561	171.4/149	895.5±0.4	48.9±1.0	15.7±0.8	73.5±0.7	10.8±0.5
$B^- \to \psi(2S)\pi^- K^0_S$	5016±292	98.1/90	891.6±2.1	44.8±6.0	23.4±4.5	71.3±4.4	5.3±2.7
$B^0 \to \psi(2S)\pi^- K^+$	13237±377	81.5/90	895.8±1.0	43.8±3.0	25.4±2.2	68.2±2.0	6.4±1.2

is $(1.2 \pm 0.6) \times 10^{-3}$ [3], and for the mode of Eq. (20) an upper limit of 1×10^{-3} (90% confidence level (c.l.)) is quoted [3]. No other information on these branching fraction values exists; the present measurements thus represent significant improvements, even in the absence of systematic error studies.

We note that the charged and neutral B meson decay rates to $J/\psi\pi^- K$ agree very well, and that this is true also for decay to $\psi(2S)\pi^- K$; also, the latter decays occur at slightly more than half the rate of the former.

VIII. THE $K\pi^-$ LEGENDRE POLYNOMIAL MOMENTS

At the beginning of Sec. VII we pointed out the need to understand the $K\pi^-$ mass dependence of the angular structure in the $K\pi^-$ system. In order to do this, we choose to represent the $K\pi^-$ angular distribution at a given $m_{K\pi^-}$ in terms of a Legendre polynomial expansion, following much the same procedure as described in Appendix A for our efficiency studies. In the notation of

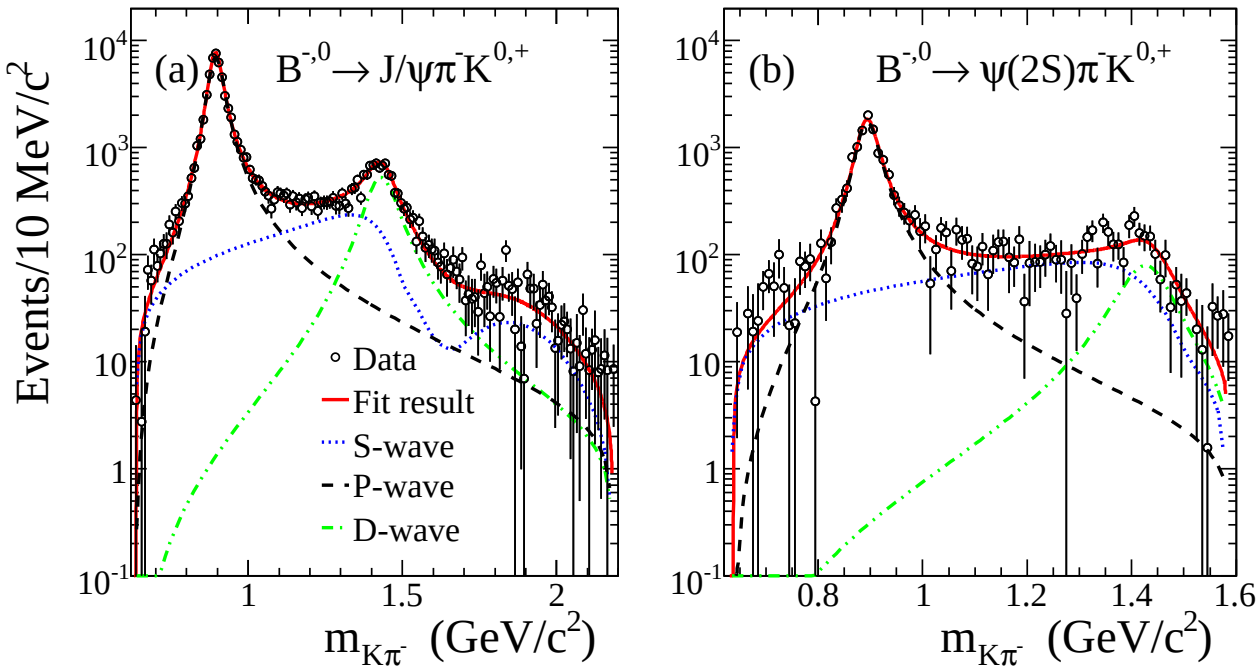

FIG. 11: The results of the fits to the $K\pi^-$ mass distributions for the combined $K\pi^-$ charge configurations (a) $B^{-,0} \to J/\psi\pi^- K^{0,+}$ and (b) $B^{-,0} \to \psi(2S)\pi^- K^{0,+}$. The data are shown as open dots, and the individual fit contributions are as indicated.

Eq. (A5), we write

$$\frac{dN}{d\cos\theta_K} = N \sum_{i=0}^{L} \langle P_i \rangle P_i(\cos\theta_K)\,, \tag{21}$$

where N is the number of events (after correction) in a small mass interval centered at $m_{K\pi^-}$, and $L = 2\ell_{max}$, where ℓ_{max} is the maximum orbital angular momentum required to describe the $K\pi^-$ system at $m_{K\pi^-}$. We can re-write Eq. (21) as

$$\frac{dN}{d\cos\theta_K} = \frac{N}{2} + \sum_{i=1}^{L} \left(N\langle P_i \rangle\right) P_i(\cos\theta_K)\,, \tag{22}$$

and extract the coefficients from the data using

$$N\langle P_i \rangle \approx \sum_{j=1}^{N} P_i(\cos\theta_{K_j})\,, \tag{23}$$

as in Appendix A. We refer to this coefficient as "the unnormalized P_i moment" in the course of our discussion. In order to incorporate the efficiency weighting and sideband subtraction procedures, we extend Eq. (23) as follows:

$$\begin{aligned} N\langle P_i \rangle \;\approx\; & \sum_{j=1}^{N} \left(\frac{1}{\epsilon_j}\right) P_i(\cos\theta_{K_j}) \\ & + \sum_{k=1}^{N_{SB}} \left(\frac{-1}{\epsilon_k}\right) P_i(\cos\theta_{K_k})\,, \end{aligned} \tag{24}$$

where N_{SB} is the number of sideband events falling in this $m_{K\pi^-}$ interval, and the efficiency values, ϵ, are obtained as described in Appendix A. For convenience, we introduce the notation $\langle P_i^U \rangle = N\langle P_i \rangle$, where the superscript U indicates that we refer to the unnormalized moment, and re-write Eq. (22) as

$$\frac{dN}{d\cos\theta_K} = \frac{N}{2} + \sum_{i=1}^{L} \langle P_i^U \rangle P_i(\cos\theta_K)\,. \tag{25}$$

An overview of the $(m_{K\pi^-}, \cos\theta_K)$ structure is provided by the rectangular Dalitz plots (see Appendix A) of Fig. 12. Data for the B decay modes of Eqs. (1) and (2) have been combined in Fig. 12(a), and data for those of Eqs. (3) and (4) have been combined in Fig. 12(b). In Fig. 12(a), the intensity for $\cos\theta_K < 0$ is stronger than for $\cos\theta_K > 0$ in the region $m_{K\pi^-} < 0.85$ GeV/c^2. A similar asymmetry is present in the $K^*(892)$ band, where in addition there is a clear decrease in intensity around $\cos\theta_K = 0$. Above ~ 1.2 GeV/c^2 the backward region is enhanced, especially in the increased intensity region at the $K_2^*(1430)$. For $m_{K\pi^-} > 1.5$ GeV/c^2 the overall intensity is significantly decreased, but the backward region of $\cos\theta_K$ continues to be favored. Despite the smaller data sample of Fig. 12(b), the backward region seems again to be favored in the $K^*(892)$ and $K_2^*(1430)$ regions, but little more can be said.

For both Fig. 12(a) and 12(b) it is necessary to examine the $m_{K\pi^-}$ dependence of the unnormalized moments in order to quantify these qualitative features.

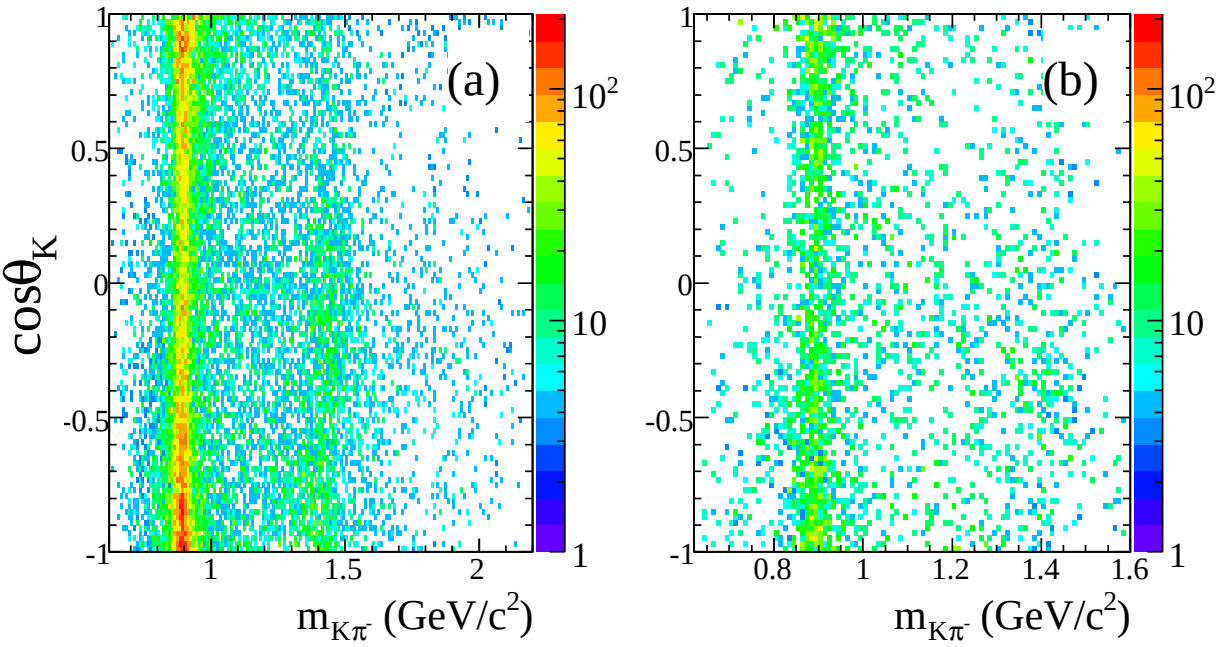

FIG. 12: The $\cos\theta_K$ versus $m_{K\pi^-}$ rectangular Dalitz plots for the combined decay modes (a) $B^{-,0} \to J/\psi\pi^- K^{0,+}$, (b) $B^{-,0} \to \psi(2S)\pi^- K^{0,+}$. The plots are obtained after efficiency weighting, but without ΔE sideband subtraction. The intensity scale is logarithmic, and is the same for both plots.

In order to facilitate discussion of the $m_{K\pi^-}$ dependence of the unnormalized moments, we first express them in terms of S-, P- and D-wave $K\pi^-$ amplitudes. These expressions have been obtained from the $B \to J/\psi\pi K$ analysis of Ref. [17], after integration over the J/ψ decay angles; they apply equally to the B meson decay to $\psi(2S)\pi K$.

For an interval of $m_{K\pi^-}$ containing N events:

$$N = \boldsymbol{S_0^2} + \boldsymbol{P_0^2} + \boldsymbol{D_0^2} + P_{+1}^2 + P_{-1}^2 + D_{+1}^2 + D_{-1}^2 \quad (26)$$

$$\begin{aligned}\langle P_1^U \rangle &= \boldsymbol{S_0 P_0 \cos(\delta_{S_0} - \delta_{P_0})} \\ &+ \boldsymbol{2\sqrt{\frac{2}{5}} P_0 D_0 \cos(\delta_{P_0} - \delta_{D_0})} \\ &+ \sqrt{\frac{6}{5}}[P_{+1}D_{+1}\cos(\delta_{P_{+1}} - \delta_{D_{+1}}) \\ &+ P_{-1}D_{-1}\cos(\delta_{P_{-1}} - \delta_{D_{-1}})]\,,\end{aligned} \quad (27)$$

$$\begin{aligned}\langle P_2^U \rangle &= \boldsymbol{\sqrt{\frac{2}{5}} P_0^2 + \frac{\sqrt{10}}{7} D_0^2} \\ &+ \boldsymbol{\sqrt{2} S_0 D_0 \cos(\delta_{S_0} - \delta_{D_0})} \\ &- \left(\frac{1}{\sqrt{10}}\left(P_{+1}^2 + P_{-1}^2\right) + \frac{5\sqrt{10}}{28}\left(D_{+1}^2 + D_{-1}^2\right)\right)\,,\end{aligned} \quad (28)$$

$$\begin{aligned}\langle P_3^U \rangle &= \boldsymbol{3\sqrt{\frac{6}{35}} P_0 D_0 \cos(\delta_{P_0} - \delta_{D_0})} \\ &- 3\sqrt{\frac{2}{35}}(P_{+1}D_{+1}\cos(\delta_{P_{+1}} - \delta_{D_{+1}}) \\ &+ P_{-1}D_{-1}\cos(\delta_{P_{-1}} - \delta_{D_{-1}}))\,,\end{aligned} \quad (29)$$

$$\langle P_4^U \rangle = \boldsymbol{\frac{3\sqrt{2}}{7} D_0^2} - \frac{2\sqrt{2}}{7}\left(D_{+1}^2 + D_{-1}^2\right)\,. \quad (30)$$

The S_i, P_i, and D_i are amplitude magnitudes and i denotes the relevant helicity; the corresponding phase angles are denoted by δ with the appropriate subscript. The helicity-zero terms, denoted in bold-face font, provide the corresponding description of $K^-\pi^+$ elastic scattering. Equations (26)-(30) define the five measurable quantities accessible to the present analysis if we restrict ourselves to S-, P-, and D-wave $K\pi^-$ amplitudes. However, the equations involve seven amplitude magnitudes and six relative phase values, and so they cannot be solved in each $m_{K\pi^-}$ interval. For this reason, we can only measure the mass dependence of the moments of the $K\pi^-$ system, and then use the results to understand how the $m_{K\pi^-}$ and $\cos\theta_K$ structure reflects into the observed $\psi\pi^-$ mass distributions, as will be discussed in Sec. IX. In the following, all $K\pi^-$ moments are sideband-subtracted and efficiency-corrected.

The dependence of $\langle P_1^U \rangle$, and of $\langle P_2^U \rangle$, on $m_{K\pi^-}$ is shown in Fig. 13. For each moment, the behavior for $\psi(2S)$ (Fig. 13(c),(d)) is very similar to that for J/ψ (Fig. 13(a),(b)), but the statistical uncertainties are significantly larger because the net analysis sample is smaller by a factor of approximately six (Table II).

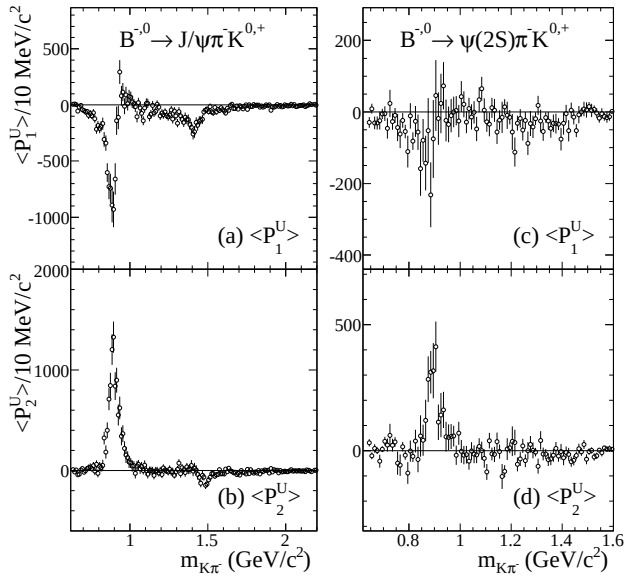

FIG. 13: The $m_{K\pi^-}$ dependence of (a) $\langle P_1^U \rangle$ and (b) $\langle P_2^U \rangle$ for $B^{0,-} \to J/\psi\pi^- K^{+,0}$; the $m_{K\pi^-}$ dependence of (c) $\langle P_1^U \rangle$ and (d) $\langle P_2^U \rangle$ for $B^{0,-} \to \psi(2S)\pi^- K^{+,0}$.

The distributions of Fig. 10 and Figs. 13-15 can be compared to those observed in Ref. [16], Fig. 6, for the $K^-\pi^+$ system produced in the reaction $K^- p \to K^-\pi^+ n$ at 11 GeV/c K^- beam momentum; the latter are representative of the moments structure of $K^-\pi^+$ elastic scattering. A striking overall feature is the strong suppression of the mass structure for $m_{K\pi^-} > 1$ GeV/c^2 relative to the $K^*(892)$ which is observed for the B meson decay processes of Eqs. (1)-(4) in comparison to $K^-\pi^+$ elastic scattering.

With this in mind, the $\langle P_1^U \rangle$ distribution of Fig. 13(a) bears a remarkable similarity to that in Ref. [16], except that the sign is reversed. This is entirely consistent with the analysis of Ref. [14], performed with a much smaller *BABAR* data sample (~ 81 fb^{-1}), which showed that the $S_0 - P_0$ relative phase of Eq. (27) differed by π from that obtained for $K^-\pi^+$ elastic scattering. In the $K^*(892)$ region, the D-wave terms in Eq. (27) should be negligible, so that the relative phase offset should yield the observed sign reversal w.r.t. $K^-\pi^+$ scattering. This sign reversal continues through the $K_2^*(1430)$ region, which suggests that $S_0 - P_0$ interference remains the dominant contribution to $\langle P_1^U \rangle$, especially since $\langle P_3^U \rangle$ is systematically positive in this region (Figs. 14(a),(c)) (Note that the first term in Eq. (29) differs by only 1.8% from the second term in Eq. (27)).

The behavior of $\langle P_2^U \rangle$ in the $K^*(892)$ region is very similar to that observed in Ref. [16], and, ignoring D-wave contributions, agrees in magnitude and sign with a calculation using the values of P_0, P_{+1}, and P_{-1} from Ref. [14]. In Ref. [16], $\langle P_2^U \rangle$ is positive and much larger at the $K_2^*(1430)$ than at the $K^*(892)$. Clearly, this is not the case in Figs. 13(b) and 13(d), where $\langle P_2^U \rangle$ is small and negative at the $K_2^*(1430)$. From Eq. (28), this could occur if S_0 is also shifted in phase by π relative to D_0, while the D_0^2 and $(D_{+1}^2 + D_{-1}^2)$ contributions to Eq. (28) essentially cancel. The latter is suggested by the observation of only a small $\langle P_4^U \rangle$ signal at the $K_2^*(1430)$ in Fig. 14(b), and the absence of signal in this region of Fig. 14(d). In Eq. (30), D_0^2 is favored 3:2 over $(D_{+1}^2 + D_{-1}^2)$, whereas in Eq. (28) the ratio is 4:5, hence the conjecture that these contributions may in effect be canceling in Figs. 13(b) and 13(d).

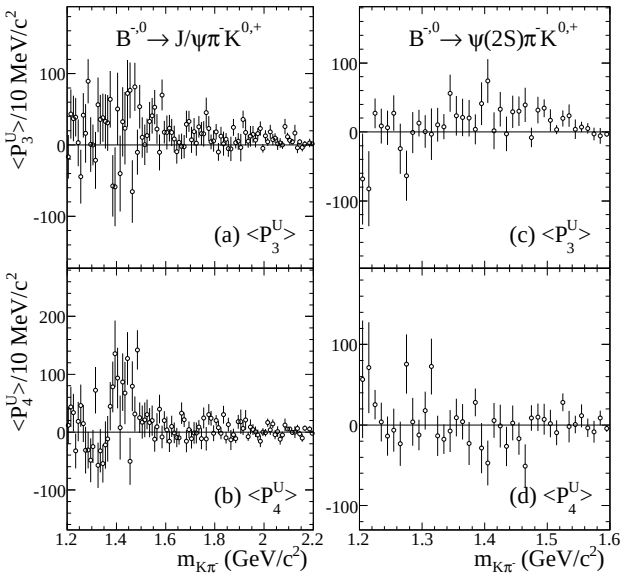

FIG. 14: The $m_{K\pi^-}$ dependence (for $m_{K\pi^-} > 1.2$ GeV/c^2) of (a) $\langle P_3^U \rangle$ and (b) $\langle P_4^U \rangle$ for $B^{0,-} \to J/\psi\pi^- K^{+,0}$; the $m_{K\pi^-}$ dependence of (c) $\langle P_3^U \rangle$ and (d) $\langle P_4^U \rangle$ for $B^{0,-} \to \psi(2S)\pi^- K^{+,0}$.

The $\langle P_3^U \rangle$ and $\langle P_4^U \rangle$ moments require that D-wave contributions be present. At the statistical level of the present analysis, we do not expect to observe such contributions for $m_{K\pi^-} < 1.2$ GeV/c^2, and so we begin the distributions of Fig. 14 at this value. In Figs. 14(a) and 14(c), $\langle P_3^U \rangle$ is systematically positive for all $m_{K\pi^-}$ mass values above 1.3 GeV/c^2. This results from the enhancement observed in Fig. 12 for $\cos\theta_K < 0$, and is similar to the behavior in Ref. [16], but at a much-reduced intensity level, as mentioned previously. The $\langle P_4^U \rangle$ moments of Fig. 14(b) and 14(d) have been discussed already. The dip to negative values at $m_{K\pi^-} \sim 1.3$ GeV/c^2 in Fig. 14(b) is interesting, since it may indicate that the

relative strength of the D_0^2 and $(D_{+1}^2 + D_{-1}^2)$ contributions to Eq. (30) varies with $m_{K\pi^-}$. The detailed amplitude analyses of the $K^*(892)$ region [14, 19] do not consider such a possibility for the P_0, P_{+1}, and P_{-1} amplitudes, but a mass-independent approach to these analyses would require a much larger data sample.

Finally, the extended $m_{K\pi^-}$ range available for the combined $B^{-,0} \to J/\psi\pi^- K^{0,+}$ data samples allows us to search for evidence of F-wave amplitude contributions associated with the $K_3^*(1780)$, which has mass ~ 1.78 GeV/c^2 and width ~ 0.20 GeV [16]. In Fig. 15(a) we show the $m_{K\pi^-}$ dependence of $\langle P_5^U \rangle$ for $m_{K\pi^-} > 1.2$ GeV/c^2, and in Fig. 15(b), the dependence of $\langle P_6^U \rangle$ for $m_{K\pi^-} > 1.5$ GeV/c^2. Interference between D- and F-wave amplitudes could yield a $\langle P_5^U \rangle$ distribution characterized by the underlying D-wave BW amplitude. For zero relative phase, the $m_{K\pi^-}$ dependence resulting from the overlap of the leading edge of the F-wave BW amplitude with the entire D-wave BW amplitude would resemble the real part of the D-wave BW. Figure 15(a) exhibits just such behavior; the intensity increases from near zero to a maximum below the $K_2^*(1430)$, passes through zero near the nominal mass value, reaches a minimum just below 1.5 GeV/c^2, returns to zero near 1.6 GeV/c^2, and has no clear structure thereafter. A $\langle P_6^U \rangle$ moment would involve F_0^2 and $(F_{+1}^2 + F_{-1}^2)$ intensity contributions of opposite sign, just as for the P- and D-waves. We see no clear signal in Fig.15(b), although the distribution is systematically negative in the region $1.7 - 1.9$ GeV/c^2, so it could be that these contributions almost cancel, as may be the case for the D-wave amplitudes. In the overall $m_{K\pi^-}$ distributions, these contributions add, and it is interesting to note that in Fig. 11(a) there is a small excess of events above the fitted curve in the region of the $K_3^*(1780)$. Our fit to the mass distribution could possibly be improved slightly in this region by including a $K_3^*(1780)$ contribution, but we do not do this at present. It seems reasonable to interpret the $m_{K\pi^-}$ dependence of $\langle P_5^U \rangle$ observed in Fig. 15(a) as indicating the presence of a $K_3^*(1780)$ amplitude, in which case this would be the first evidence for B meson decay to a final state including a spin three resonance.

In summary, the angular structures observed for the $K\pi^-$ systems produced in $B^{-,0} \to J/\psi\pi^- K^{0,+}$ and $B^{-,0} \to \psi(2S)\pi^- K^{0,+}$ show interesting features, which can be well understood on the basis of the expected $K\pi^-$ amplitude contributions. Moreover, the main features agree well between the J/ψ and $\psi(2S)$ modes, taking account of the statistical limitations of the latter data sample.

IX. REFLECTION OF $K\pi^-$ STRUCTURE INTO THE $\psi\pi^-$ MASS DISTRIBUTIONS

We now investigate the extent to which reflection of the $K\pi^-$ mass and angular structures described in Secs. VII and VIII are able to reproduce the efficiency-corrected and sideband-subtracted $\psi\pi^-$ mass distributions.

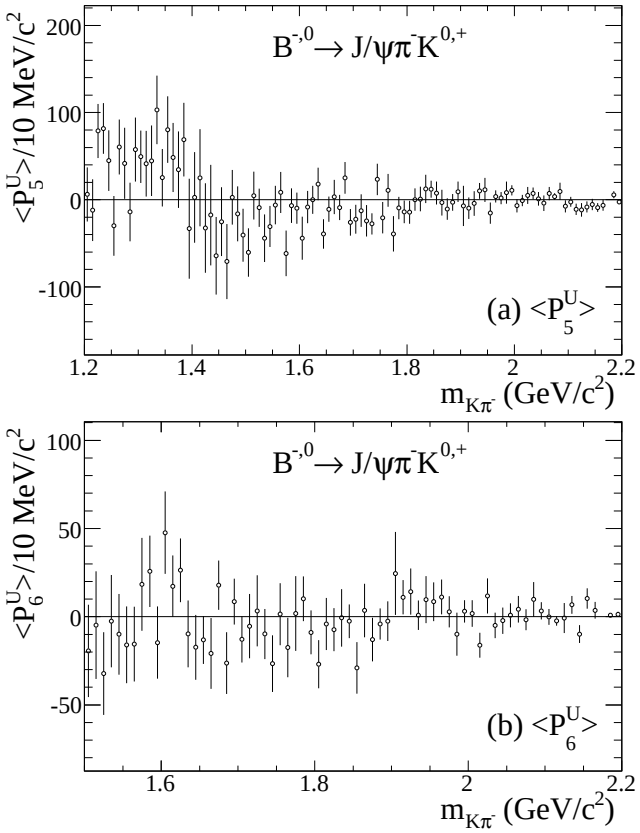

FIG. 15: (a) The $m_{K\pi^-}$ dependence of $\langle P_5^U \rangle$ for $m_{K\pi^-} > 1.2$ GeV/c^2 for $B^{0,-} \to J/\psi\pi^- K^{+,0}$; (b) the $m_{K\pi^-}$ dependence of $\langle P_6^U \rangle$ for $m_{K\pi^-} > 1.5$ GeV/c^2 for $B^{0,-} \to J/\psi\pi^- K^{+,0}$.

We do this by using a MC generator which initially creates large samples of unit weight $B^{-,0} \to \psi\pi^- K^{0,+}$ events with the correct B meson production angular distribution in the overall c.m. frame, and distributed in $K\pi^-$ mass according to the fit functions obtained as described in Sec. VII. The distribution in $\cos\theta_K$ is uniform at each value of $m_{K\pi^-}$, and so is described by

$$\frac{dN}{d\cos\theta_K} = \frac{N}{2}\,, \tag{31}$$

which is just Eq. (25) with no angular structure.

Since we are now dealing with efficiency-corrected distributions, and since mass resolution cannot generate local structure (Fig. 6), we need not subject the generated events to detector response simulation and subsequent event reconstruction. Consequently we can create very large MC samples.

The $K\pi^-$ mass distributions generated in this way for $B^{-,0} \to J/\psi\pi^- K^{0,+}$ and $B^{-,0} \to \psi(2S)\pi^- K^{0,+}$ are shown in Figs. 16(a) and 16(b), respectively. Each distribution contains ten million events, and has been normalized to the total number of events in the corresponding corrected data sample; each represents the relevant fit

function of Fig. 11 very well. We can use these events to create $\psi\pi^-$ mass distributions according to any desired selection criteria, and we provide several examples of this later.

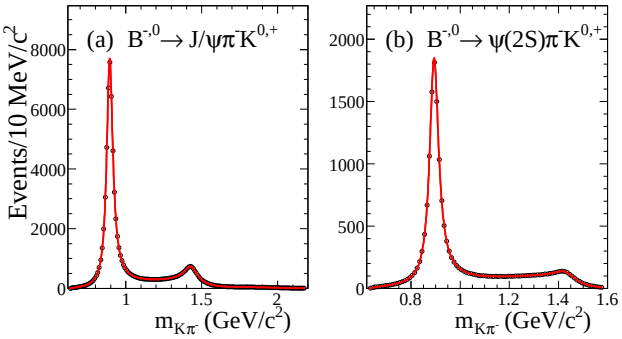

FIG. 16: The $K\pi^-$ mass distributions generated according to the $K\pi^-$ fit functions of Fig. 11 for (a) $B^{-,0}\to J/\psi\pi^-K^{0,+}$ and (b) $B^{-,0}\to\psi(2S)\pi^-K^{0,+}$. Each distribution contains ten million events, normalized to the total number of events observed in the corrected data sample (Fig. 11).

However, in Sec. VIII we showed that there is a great deal of angular structure in the $K\pi^-$ system, as represented by the $m_{K\pi^-}$ dependence of the $\langle P_i^U\rangle$ moments, and this affects the reflection from the $K\pi^-$ system into the $\psi\pi^-$ mass distribution.

We take this $K\pi^-$ angular structure into account by returning to Eq. (25), removing a factor of $N/2$ on the right side, and so obtaining

$$\frac{dN}{d\cos\theta_K}=\frac{N}{2}\left(1+\sum_{i=1}^{L}(\frac{2}{N})\langle P_i^U\rangle P_i(\cos\theta_K)\right)\,, \quad (32)$$

i.e.

$$\frac{dN}{d\cos\theta_K}=\frac{N}{2}\left(1+\sum_{i=1}^{L}\langle P_i^N\rangle P_i(\cos\theta_K)\right)\,, \quad (33)$$

where

$$\langle P_i^N\rangle=\frac{2}{N}\langle P_i^U\rangle \quad (34)$$

is defined to be the "the normalized P_i moment". We can thus incorporate the measured $K\pi^-$ angular structure into our generator by giving weight w_j to the j^{th} event generated, where

$$w_j=1+\sum_{i=1}^{L}\langle P_i^N\rangle P_i(\cos\theta_{K_j})\,. \quad (35)$$

The $\langle P_i^N\rangle$ are evaluated for the $m_{K\pi^-}$ value of the j^{th} event by linear interpolation of the values obtained by normalizing the $\langle P_i^U\rangle$ of Figs. 13-15 according to Eq. (34).

The results are shown in Figs. 17-19, where we have used modified mass intervals in order to reduce statistical fluctuation. We interpolate linearly using the lines connecting the measured values. In order to take into account the statistical uncertainties, we also interpolate using lines connecting the $+1\sigma$ error values, and lines connecting the -1σ error values, as shown by the shaded regions in each plot.

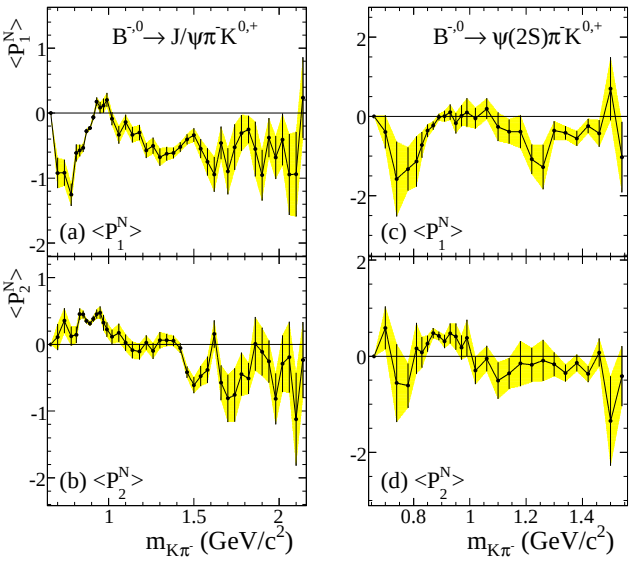

FIG. 17: The normalized moments corresponding to Fig. 13 obtained by using Eq. (34). Mass intervals have been combined in order to reduce statistical fluctuations. The lines indicate the linear interpolations used in weighting the MC events. The shaded regions indicate the $\pm1\sigma$ variations used to account of statistical uncertainties.

The $\psi\pi^-$ mass distributions for the entire $K\pi^-$ mass range for the decay modes $B^{-,0}\to J/\psi\pi^-K^{0,+}$ and $B^{-,0}\to\psi(2S)\pi^-K^{0,+}$ are shown in Fig. 20(a) and Fig. 20(b), respectively. The points represent the data after correcting for efficiency and subtracting the events in the ΔE sideband. The dashed curves show the reflection from $K\pi^-$ assuming a flat $\cos\theta_K$ distribution. The solid curves are obtained by weighting each event according to Eq. (35). The shaded bands associated with the solid curves indicate the effect of interpolation using $\pm1\sigma$ normalized moment values, as described above.

We emphasize that the absolute normalization of the curves shown in Figs. 20(a) and 20(b) is established by the scale factor used to normalize each of our ten-million-event MC samples to the corresponding corrected number of events, as shown in Figs. 16(a) and 16(b), respectively.

Comparison of the dashed and solid curves of Fig. 20 shows that it is important to modulate the $\cos\theta_K$ distributions using the normalized moment weights of Eq. (35). Since the individual $P_i(\cos\theta_K)$ functions integrate to zero over $\cos\theta_K$, the incorporation of the w_j weights does not affect the distributions of Fig. 16. This also means that the associated dashed and solid curves of Fig. 20 integrate to the same total number of events.

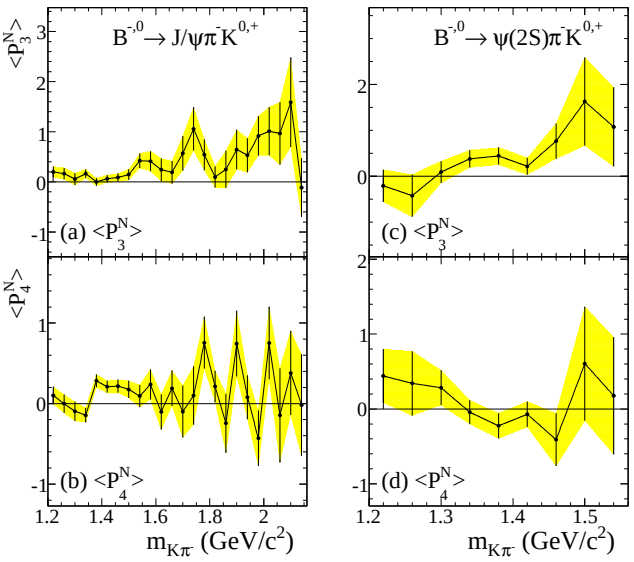

FIG. 18: The normalized moments corresponding to Fig. 14 obtained by using Eq. (34). Mass intervals have been combined in order to reduce statistical fluctuations. The lines indicate the linear interpolations used in weighting the MC events. The shaded regions indicate the $\pm 1\sigma$ variations used to account of statistical uncertainties.

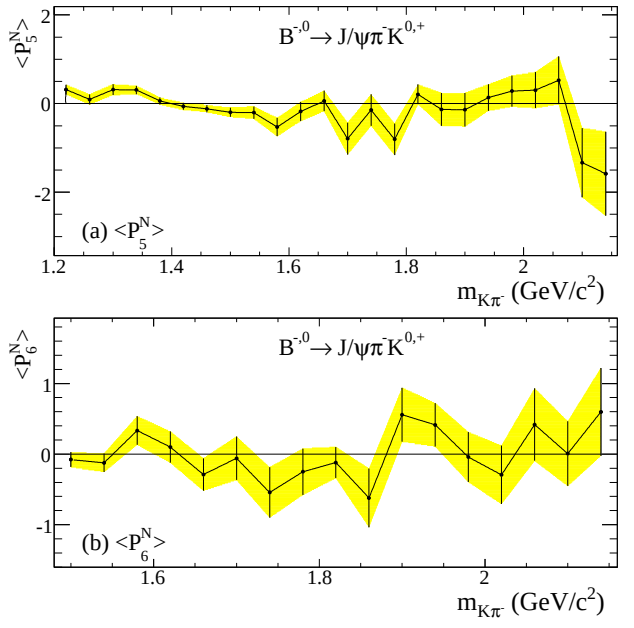

FIG. 19: The normalized moments corresponding to Fig. 15 obtained by using Eq. (34). Mass intervals have been combined in order to reduce statistical fluctuations. The lines indicate the linear interpolations used in weighting the MC events. The shaded regions indicate the $\pm 1\sigma$ variations used to account of statistical uncertainties.

The reasons for the enhancement of the solid curves at high $\psi\pi^-$ mass values, and their suppression at lower mass values are made clear by the rectangular Dalitz plots of Figs. 21(a) and 21(b). We plot $\cos\theta_\psi$ against $m_{\psi\pi^-}$, where $\cos\theta_\psi$ is the normalized dot-product of the $\psi\pi^-$ three-momentum vector in the parent B meson rest frame and the ψ three-momentum vector in the $\psi\pi^-$ rest frame. A guide to the structures observed in these plots is provided by Figs. 21(c) and 21(d), where we indicate the locus of the $K^*(892)$ band ($0.795 - 0.995$ GeV/c^2) and that of the $K_2^*(1430)$ band ($1.330 - 1.530$ GeV/c^2), as chosen in Ref. [5]; in addition, we label regions (A)-(E), defined in Sec. X. The dashed vertical lines indicate the $Z(4430)^-$ region from Ref. [5]. The high-$m_{\psi\pi^-}$ region of each of these bands corresponds to $\cos\theta_K < 0$, and in Fig. 21(a) this region is clearly populated preferentially for both K^* bands, and even for the $K\pi^-$ mass range in between. This corresponds to the backward-forward asymmetry observed in Fig. 12, and to the negative values observed for $\langle P_1^U \rangle$ in Fig. 13(a), and to the positive values of $\langle P_3^U \rangle$ in Fig. 14(a). These high-$m_{\psi\pi^-}$ enhancements are compensated by the low-$m_{\psi\pi^-}$ suppression of the solid curve relative to the dashed curve in Fig. 20(a), since the integral along any $m_{K\pi^-}$ locus is independent of the $\cos\theta_K$ distribution. Similar behavior is observed for Fig. 20(b), but at a reduced statistical level. Backward-forward asymmetry is observed in Fig. 12(b), where $\langle P_1^U \rangle$ is primarily negative in Fig. 13(c) and $\langle P_3^U \rangle$ is positive in Fig. 14(c), so that the net effect on the $\psi\pi^-$ mass distribution of Fig. 20(b) is much the same as in Fig. 20(a).

In Figs. 20(c) and 20(d), we show the residuals (data - solid curves) for the distributions in Figs. 20(a) and 20(b), respectively. The dashed vertical lines indicate $m_{\psi\pi^-} = 4.433$ GeV/c^2 [5].

There is an excess of events in Fig. 20(c) for $m_{J/\psi\pi^-} \sim 4.61$ GeV/c^2, as well as in Fig. 25(b) and Fig. 26(c) below. The effect is associated with the $K^*(892)$ region of $K\pi^-$ mass (Fig. 24(b)), for which the $m_{J/\psi\pi^-}$ distribution decreases steeply in the high-mass region. The mass resolution there is ~ 9 MeV/c^2 (Fig. 6(a),(c)) and we have not incorporated this into our calculations. For this reason, the calculated curve falls systematically below the data, hence yielding a spurious peak in the residual distribution. For the corresponding $m_{\psi(2S)\pi^-}$ distributions, the mass resolution is ~ 4 MeV/c^2 (Fig. 6(b),(d)) at ~ 4.6 GeV/c^2, the statistical fluctuations are larger, and no similar effect is observed (Figs. 20(d), 25(g), and 26(d)). Apart from this, the distribution of the residuals shows no evidence of statistically significant departure from zero at any $J/\psi\pi^-$ mass value.

In Fig. 20(b), and correspondingly in Fig. 20(d), the small excess of events at ~ 4.48 GeV/c^2 provides the only indication of a narrow signal. As shown in Sec. XI B, this yields a 2.7σ enhancement with mass ~ 4.476 GeV/c^2 and width consistent with that reported in Ref. [5]. The dot-dashed curve in Fig. 20(b) was obtained from the dashed curve by modulating the $K\pi^-$ angular distribution using instead the normalized $K\pi^-$ moments from

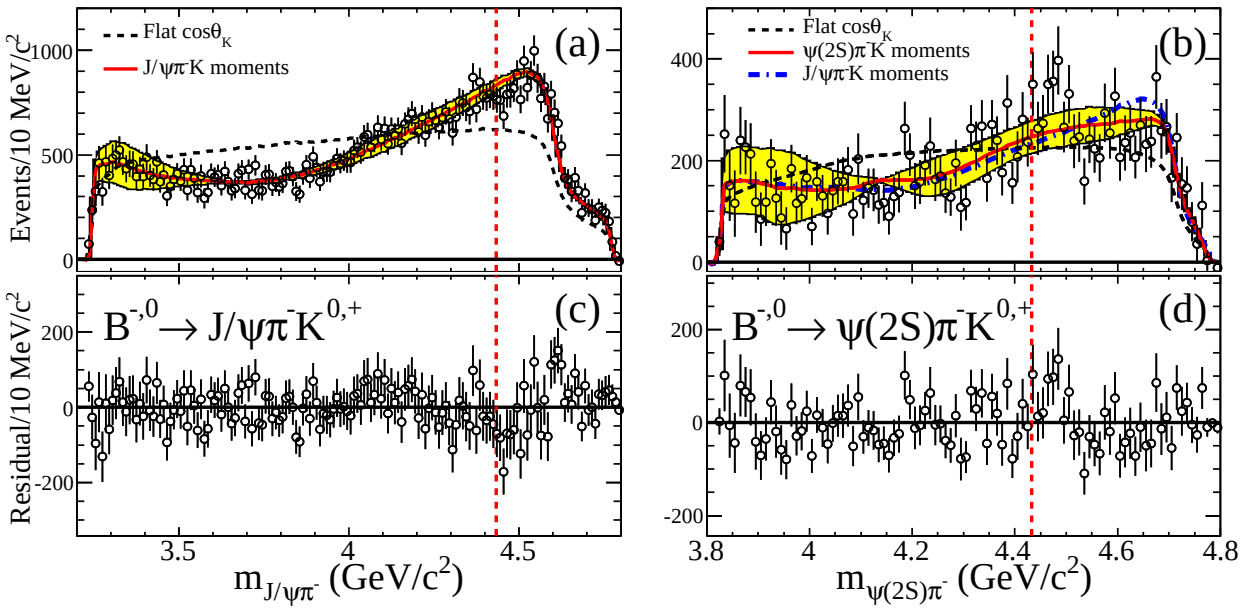

FIG. 20: The $\psi\pi^-$ mass distributions for the combined decay modes (a) $B^{-,0} \to J/\psi\pi^- K^{0,+}$ and (b) $B^{-,0} \to \psi(2S)\pi^- K^{0,+}$. The points show the data after efficiency correction and ΔE sideband subtraction. The dashed curves show the $K\pi^-$ reflection for a flat $\cos\theta_K$ distribution, while the solid curves show the result of $\cos\theta_K$ weighting. The shaded bands represent the effect of statistical uncertainty on the normalized moments. In (b), the dot-dashed curve indicates the effect of weighting with the normalized $J/\psi\pi^- K$ moments. The dashed vertical lines indicate the value of $m_{\psi\pi^-} = 4.433$ GeV/c^2. In (c) and (d), we show the residuals (data-solid curve) for (a) and (b), respectively.

the $B^{-,0} \to J/\psi\pi^- K^{0,+}$ data, which show no evidence of a $Z(4430)^-$ signal. This curve and the solid curve differ only slightly in the range ~ 4.2 GeV/c^2 to ~ 4.55 GeV/c^2, so that the $K\pi^-$ background function at ~ 4.48 GeV/c^2 is not very sensitive to the modulation procedure, nor to the presence of a small, narrow $m_{\psi(2S)\pi^-}$ enhancement (see Sec. XI B for a quantitative discussion).

We conclude that the $m_{\psi(2S)\pi^-}$ distribution of Fig. 20(b), and the residual distribution of Fig. 20(d), do not provide confirmation of the $Z(4430)^-$ signal reported in Ref. [5].

X. COMPARISON TO THE BELLE RESULTS

We now compare our results to those obtained by Belle for $B \to \psi(2S)\pi^- K$ [5].

A. The $\psi\pi^-$ mass resolution

In Sec. V we showed (Fig. 6) our mass resolution dependence on Q-value, and obtained HWHM ~ 4 MeV/c^2 for the $\psi(2S)\pi^-$ system at the $Z(4430)^-$. In Ref. [5], it is stated only that the mass resolution is 2.5 MeV/c^2. Since the width of the $Z(4430)^-$ is ~ 45 MeV [5], mass resolution should not be an issue for the comparison of similar data samples (see Sec. X E).

B. Efficiency

We have made a detailed study of efficiency over each Dalitz plot for each J/ψ and $\psi(2S)$ decay mode separately (Sec. VI), and have identified efficiency losses associated with low-momentum pions and kaons in the laboratory frame (Fig. 9). We illustrate the effect of such losses on the $m_{\psi\pi^-}$ distributions using our ten-million-event $B^{-,0} \to \psi\pi^- K^{0,+}$ samples weighted to take account of the $K\pi^-$ angular structure (Sec. IX). In Fig. 22 we show the $\psi\pi^-$ distributions obtained as for Fig. 20 (solid curves). We then require that the momentum of the π be less than 100 MeV/c in the laboratory frame (Fig. 9) and obtain the shaded distributions in the $m_{\psi\pi^-}$ threshold regions. Similarly, the requirement that the kaon momentum be less than 250 MeV/c in the laboratory frame (Fig. 9) yields the cross-hatched regions near maximum $\psi\pi^-$ mass [20]. It follows that the regions of lower efficiency discussed in Appendix A should have no significant effect on the region of the $Z(4430)^-$.

As a direct check of the effect of our efficiency-correction procedure, we show our $m_{\psi\pi^-}$ distributions before and after correction in Figs. 23(a),(b)

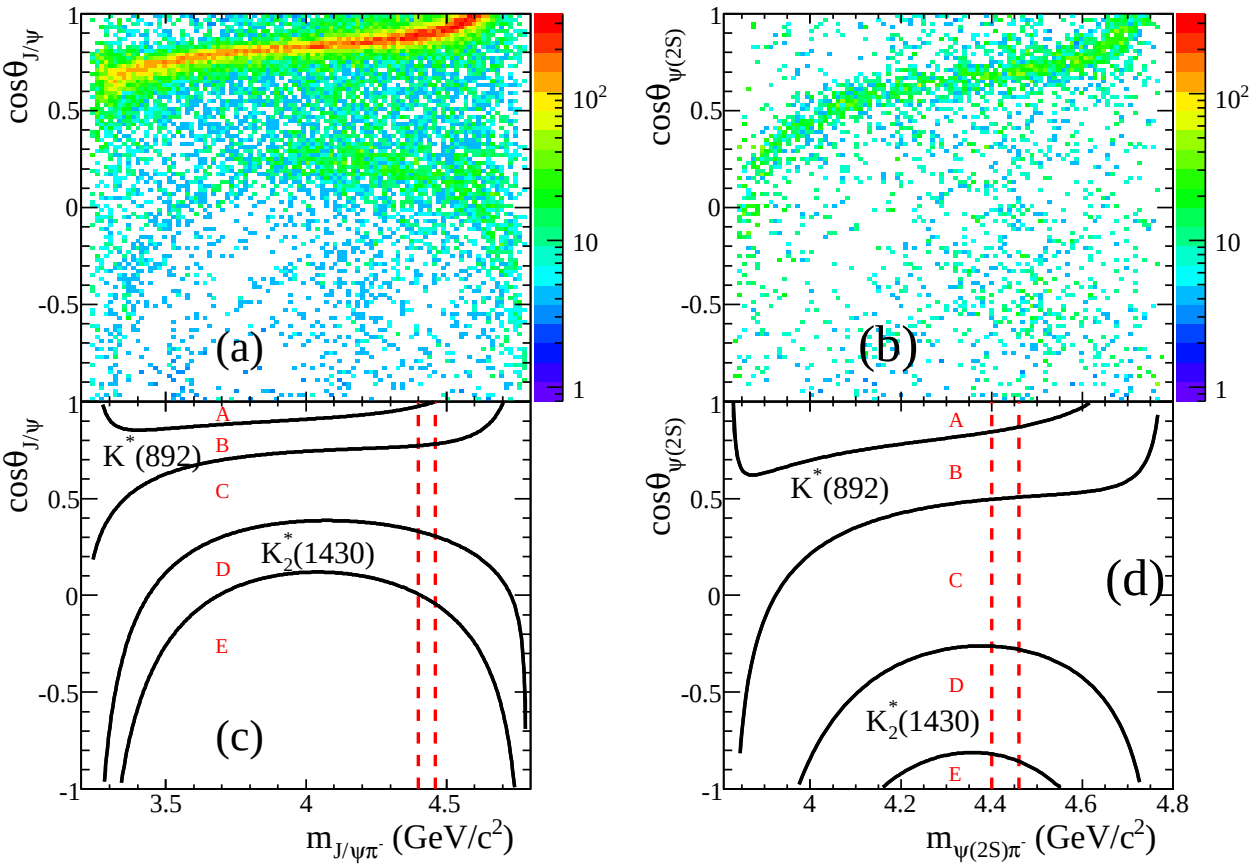

FIG. 21: The $\cos\theta_\psi$ versus $m_{\psi\pi^-}$ rectangular Dalitz plots for (a) $B^{-,0} \to J/\psi\pi^- K^{0,+}$, and (b) $B^{-,0} \to \psi(2S)\pi^- K^{0,+}$; (c) and (d), the corresponding plots indicating the loci of the $K^*(892)$ and $K_2^*(1430)$ resonance bands defined in the text; regions A-E, defined by Eqs. (36)-(40), are indicated. The dashed vertical lines show the mass range $4.400 < m_{\psi\pi^-} < 4.460$ GeV/c^2.

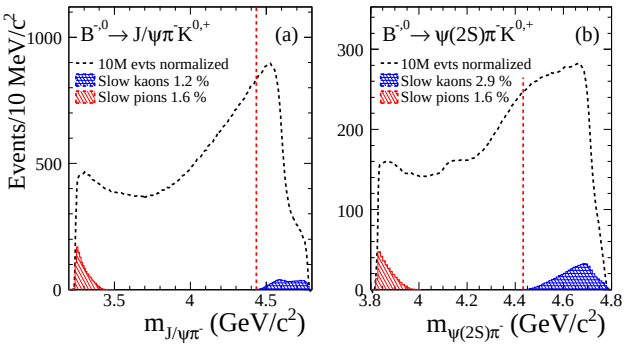

FIG. 22: (a) The curve of Fig. 20(a), and (b) that of Fig. 20(b), obtained by $\cos\theta_K$ weighting; the shaded regions near threshold correspond to $P(\pi^-) < 0.1$ GeV/c in the laboratory frame, while the cross-hatched regions near maximum $\psi\pi^-$ mass represent $P(K) < 0.25$ GeV/c in the laboratory frame; the dashed vertical lines indicate $m_{\psi\pi^-} = 4.433$ GeV/c^2.

and 23(d),(e) for $B^{-,0} \to J/\psi\pi^- K^{0,+}$ and $B^{-,0} \to \psi(2S)\pi^- K^{0,+}$, respectively. Then in Fig. 23(c) and 23(f) we show the ratio of the uncorrected and corrected distributions as a measure of average efficiency. As expected, the average value decreases rapidly near threshold, and near the maximum value for both distributions. Away from these regions, the efficiency increases slowly with increasing mass. We conclude that our event reconstruction efficiency should have no effect on any $Z(4430)^-$ signal in our data.

In Fig. 23(f) we show the result of a linear fit, excluding the regions $m_{\psi(2S)\pi^-} < 3.9$ GeV/c^2 and $m_{\psi(2S)\pi^-} > 4.71$ GeV/c^2, which are seriously affected by the loss of low momentum pions and kaons, respectively. The fitted efficiency value increases from 13.7 % to 15.0 % over the fitted region. The low-efficiency regions are excluded when we compare our uncorrected $m_{\psi(2S)\pi^-}$ distribution to that from Belle (Sec. X E). This is due to the fact that for both experiments the reconstruction efficiency for very low momentum charged-particle tracks in the laboratory frame decreases rapidly to zero (*cf.* Fig. 9).

There is no detailed discussion of efficiency in Ref. [5].

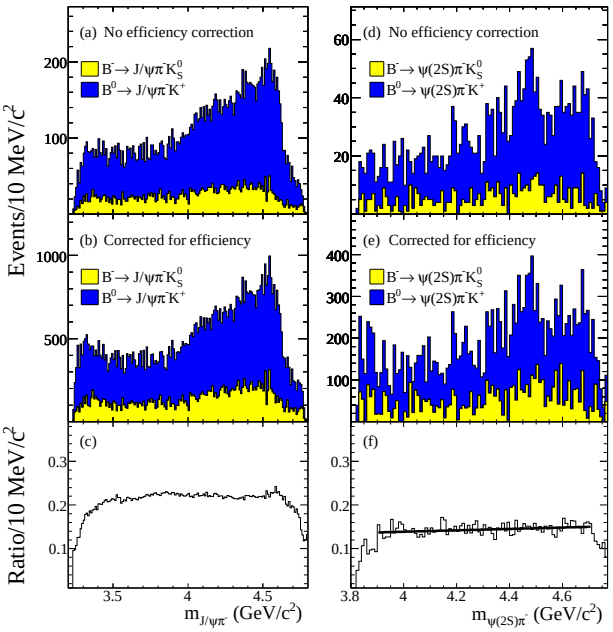

FIG. 23: The cumulative $\psi\pi^-$ mass distributions for the K^0_S and K^+ decay modes (a) and (d) before, and (b) and (e) after, efficiency correction. The ratio of uncorrected to corrected data is shown in (c) and (f). The fitted line in (f) is described in the text.

C. The $K\pi^-$ mass and $\cos\theta_K$ structures

In Ref. [5], the $K^*(892)$ and $K^*_2(1430)$ regions of the Dalitz plot are removed, and the remaining non-$Z(4430)^-$ contribution to the $m_{\psi(2S)\pi^-}$ mass distribution is described by a second-order polynomial in $m_{\psi(2S)\pi^-}$ multiplied by the momentum of the $\psi(2S)$ in the $\psi(2S)\pi^-$ rest frame and by the factor $\sqrt{m_{max} - m_{\psi(2S)\pi^-}}$; for two-out-of-three phase space, this latter factor should be the momentum of the recoil K in the B rest frame. Also, the ΔE sideband contributions are not subtracted prior to their fit. There is no discussion of a possible description of the background in terms of $K\pi^-$ mass and angular structures.

In our analysis, we have considered the effect of the $K\pi^-$ mass and $\cos\theta_K$ structures (Sec. VII and Sec. VIII), and have shown how the observed features affect the $\psi\pi^-$ mass distributions in Sec. IX. The resulting dashed curves of Fig. 22 cannot be described in terms of second-order polynomials. However, each corresponds to a projection of the entire Dalitz plot. In order to make a direct comparison to the Belle data, we investigate the relevant regions of $K\pi^-$ mass in the following section.

D. Regions of $K\pi^-$ mass

The $\psi(2S)\pi$ mass distribution shown in Fig. 2 of Ref.[5] has a "K^* veto" applied. This means that events within 100 MeV/c^2 of the $K^*(892)$ or the $K^*_2(1430)$ have been removed, and hence that the $K\pi^-$ mass range has, in effect, been divided into five regions, as follows:

$$\text{region A}: \quad m_{K\pi^-} < 0.795 \text{ GeV/c}^2\,, \tag{36}$$
$$\text{region B}: \quad 0.795 < m_{K\pi^-} < 0.995 \text{ GeV/c}^2\,, \tag{37}$$
$$\text{region C}: \quad 0.995 < m_{K\pi^-} < 1.332 \text{ GeV/c}^2\,, \tag{38}$$
$$\text{region D}: \quad 1.332 < m_{K\pi^-} < 1.532 \text{ GeV/c}^2\,, \tag{39}$$
$$\text{region E}: \quad m_{K\pi^-} > 1.532 \text{ GeV/c}^2\,. \tag{40}$$

These regions are labeled in Fig. 21(c) and Fig. 21(d). The $\psi(2S)$ mass distribution of Ref. [5] thus contains events (with sideband contribution) from regions A, C, and E.

In Fig. 24 we show the corrected $m_{\psi\pi^-}$ distributions for regions A-E of $K\pi^-$ mass. The solid curves and shaded bands correspond to those in Fig. 20, with the same overall normalization constants as obtained for Fig. 16, *i.e.*, there is no renormalization in the separate $K\pi^-$ mass regions. In Figs. 24(f)-(j), the dot-dashed curves were obtained using the normalized moments from $B^{-,0} \to J/\psi\pi^- K^{0,+}$ in conjunction with Eq. (35). For regions A and B, there is almost no difference between the solid and dot-dashed curves, while in the other regions the differences are less than, or of the order of, the statistical fluctuations in the associated data. The residuals (obtained by subtracting the solid curves from the data) corresponding to Fig. 24 are shown in Fig. 25, and show no evidence of structure. In Figs. 26 and Fig. 27 we make similar comparisons for the combined data in the K^* regions (B and D), and for the K^*-veto region (A, C, and E). Again the residuals reveal no significant structure.

E. Direct comparison

The $\psi(2S)\pi^-$ mass distribution of Fig. 28(a) is a reproduction of that in Ref. [5], except for the addition of error bars [21]. In Fig. 28(b) we show the equivalent distribution for our combined analysis samples for the B meson decay processes of Eqs. (3) and (4) for the K^*-veto region (A, C, and E). The mass intervals are the same as for Fig. 28(a), but no efficiency-correction has been performed. As mentioned in Sec. X C, when we make quantitative comparisons between Fig. 28(a) and Fig. 28(b) we exclude the low-efficiency regions near threshold and at high mass, and use only the region $3.9 < m_{\psi(2S)\pi^-} < 4.71$ GeV/c^2. We make a global comparison of the data samples in Table IV. The *BABAR* sample contains $\sim 8\%$ more background than does the Belle sample. The net signal ratio is 1.18 ± 0.09 in favor of Belle, although the corresponding integrated luminosity ratio is 1.46. It follows that for *BABAR*, net signal per

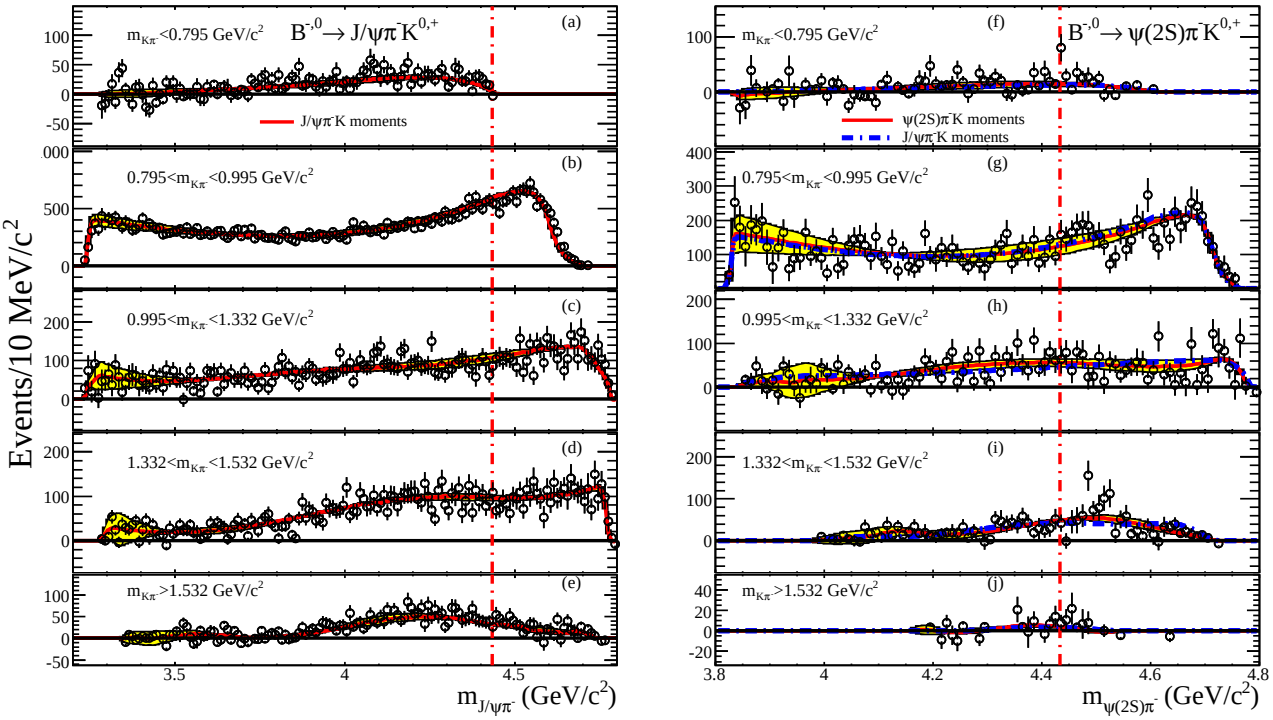

FIG. 24: The $\psi\pi^-$ mass distributions in regions A-E of $K\pi^-$ mass for the combined decay modes (a-e) $B^{-,0} \to J/\psi\pi^- K^{0,+}$, and (f-j) $B^{-,0} \to \psi(2S)\pi^- K^{0,+}$; the open dots represent the data, and the solid curves and shaded bands are as in Fig. 20, but calculated for the relevant $K\pi^-$ mass region using the same overall normalization constant as for Fig. 16. In (f-j), the dot-dashed curves are obtained using $K\pi^-$ normalized moments for $B^{-,0} \to J/\psi\pi^- K^{0,+}$ in Eq. (35), instead of those from $B^{-,0} \to \psi(2S)\pi^- K^{0,+}$; the dot-dashed vertical lines indicate $m_{\psi\pi^-} = 4.433$ GeV/c^2.

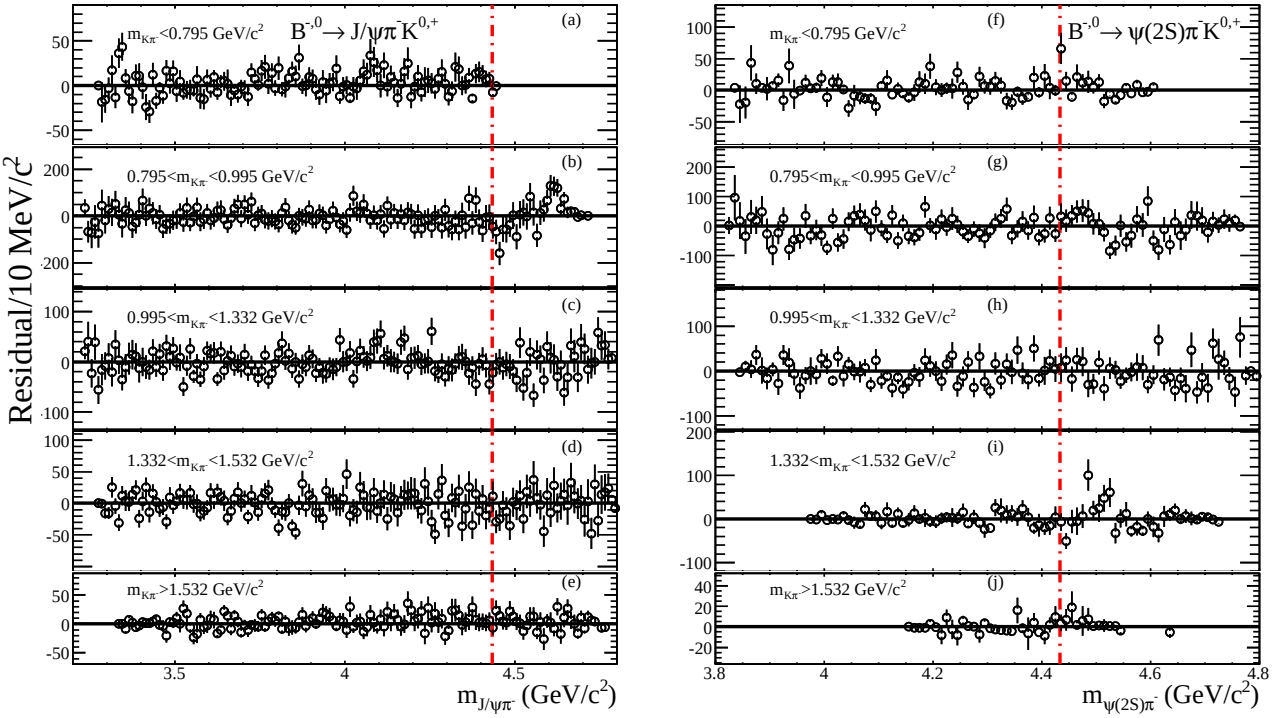

FIG. 25: The residuals (data - solid curve) corresponding to Fig. 24; the dot-dashed vertical lines indicate $m_{\psi\pi^-} = 4.433$ GeV/c^2.

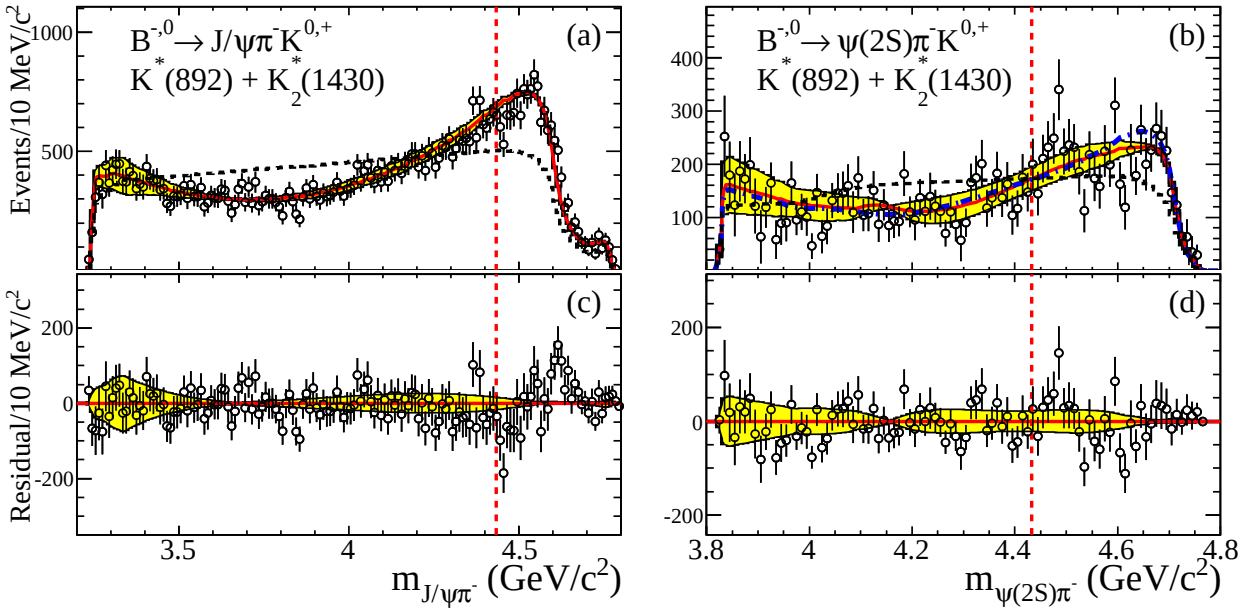

FIG. 26: The $\psi\pi^-$ mass distributions for (a) $B^{-,0} \to J/\psi\pi^- K^{0,+}$, and (b) $B^{-,0} \to \psi(2S)\pi^- K^{0,+}$, for $m_{K\pi^-}$ regions B and D combined; the open dots represent the data, the solid, dashed, and dot-dashed curves, and the shaded bands, correspond to those of Fig. 20(a),(b); (c) and (d), the corresponding residual distributions. The dashed vertical lines indicate $m_{\psi\pi^-} = 4.433$ GeV/c^2.

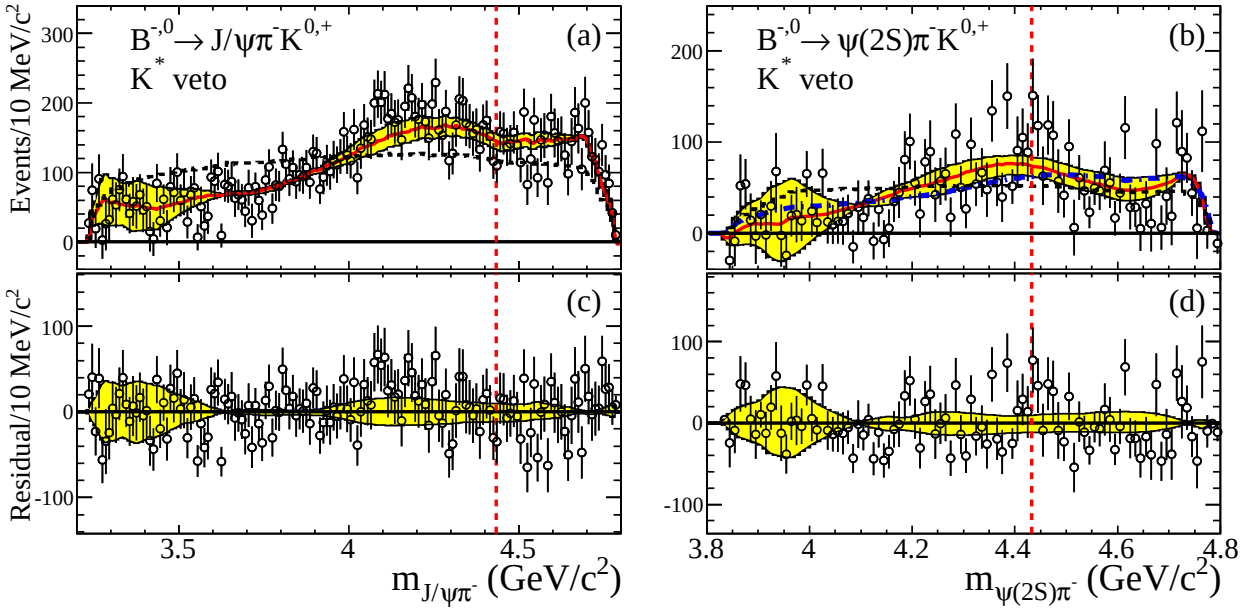

FIG. 27: The $\psi\pi^-$ mass distributions for (a) $B^{-,0} \to J/\psi\pi^- K^{0,+}$, and (b) $B^{-,0} \to \psi(2S)\pi^- K^{0,+}$, for $m_{K\pi^-}$ regions A, C, and E, combined; the open dots represent the data, the solid, dashed, and dot-dashed curves, and the shaded bands, correspond to those of Fig. 20(a),(b); (c) and (d), the corresponding residual distributions. The dashed vertical lines indicate $m_{\psi\pi^-} = 4.433$ GeV/c^2.

unit luminosity is ~ 1.34, while for Belle it is 1.08, and that this significant increase in signal yield comes at the cost of only a modest increase in background level. For both experiments the background distribution increases toward threshold, and differs markedly in $\psi(2S)\pi^-$ mass dependence from the signal.

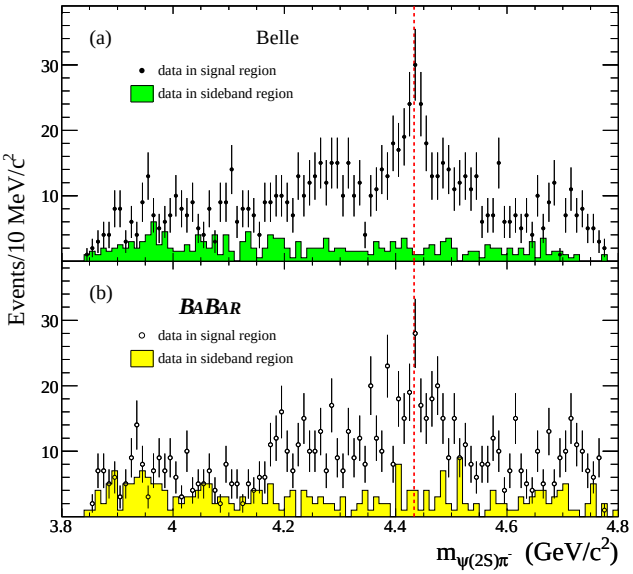

FIG. 28: a) The $\psi(2S)\pi^-$ mass distribution after K^* veto from Ref. [5]; the data points represent the signal region (we have assigned $\sqrt{N}$ errors at present), and the shaded histogram represents the background contribution estimated from the ΔE sideband regions; b) shows the corresponding distribution from the *BABAR* analysis. The dashed vertical line indicates $m_{\psi(2S)\pi^-} = 4.433$ GeV/c^2.

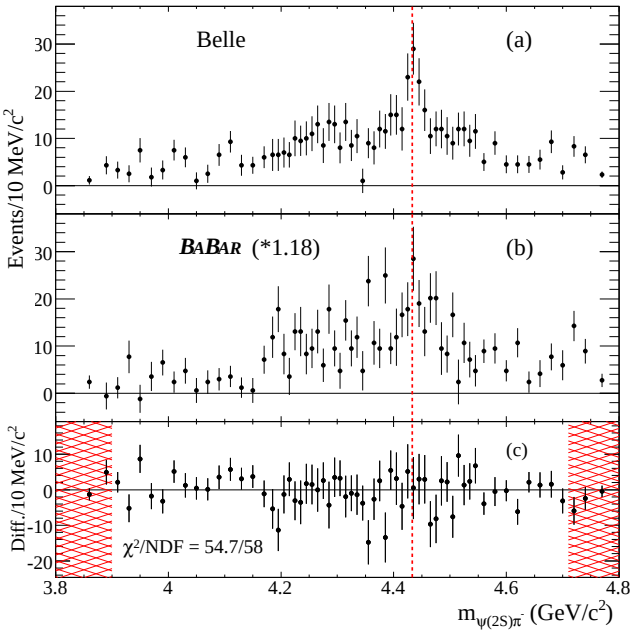

FIG. 29: a) The distribution of Fig. 28(a) after combining mass intervals for $m_{\psi(2S)\pi^-} < 4.18$ GeV/c^2 and $m_{\psi(2S)\pi^-} > 4.55$ GeV/c^2, and carrying out sideband subtraction. b) The distribution of Fig. 28(b) after following the same procedure, and in addition scaling by 1.18, as described in the text. c) The difference, (a)-(b), where the errors have been combined in quadrature; $\chi^2/NDF = 54.7/58$ (Probability=59.9%) excluding the low-efficiency regions (cross-hatched).

We have shown our efficiency-corrected and sideband-subtracted mass distribution corresponding to Fig. 28(b) in Fig. 27(b), and should compare the latter to the equivalent Belle distribution. However, this is not available, and so we make do with the distributions of Fig. 28 instead. In order to justify the use of $\sqrt{N}$ error assignments, we combine adjacent mass intervals for $m_{\psi(2S)\pi^-} < 4.18$ GeV/c^2 and $m_{\psi(2S)\pi^-} > 4.55$ GeV/c^2 so that we obtain at least ten events (signal + sideband) in each mass interval. We then create the sideband-subtracted distributions of Fig. 29(a) and Fig. 29(b) from the data of Fig. 28(a) and Fig. 28(b), respectively. In Fig. 29(b), we have scaled our data by the factor 1.18 to compensate for the statistical difference between the experiments. In Fig. 29(c) we show the result of subtracting the distribution of Fig. 29(b) from that of Fig. 29(a), with errors combined in quadrature. There is no evidence of any statistically significant difference, in particular near $m_{\psi(2S)\pi^-} = 4.433$ GeV/c^2, indicated by the dashed vertical line. If the low-efficiency (Fig. 23(f)) cross-hatched regions of Fig. 29(c) are excluded, the χ^2-value for the remaining region is found to be 54.7 for 59 mass intervals. There is one normalization constant (1.18), so that the comparison yields $\chi^2/NDF = 54.7/58$, with corresponding probability 59.9%.

We conclude that the Belle and *BABAR* distributions of Fig. 29 are statistically consistent. We have shown in Fig. 20 and Figs. 24-27 that all of our corrected $\psi\pi^-$ distributions are well-described by reflections of the mass and angular structures of the $K\pi^-$ system. We refer to this as our $K\pi^-$ background, and in Sec. XI we quantify the extent to which an additional $Z(4430)^-$ signal is required to describe the corrected *BABAR* $\psi\pi^-$ mass distributions.

We have mentioned previously that it is the backward-forward asymmetry in the $K\pi^-$ angular distribution as a function of $m_{K\pi^-}$ which yields the high mass enhancements seen in our $\psi\pi^-$ mass distributions. We show this effect explicitly in Fig. 30, where we plot the distribution of $\cos\theta_\pi = -\cos\theta_K$ for regions A, C, and E of $K\pi^-$ mass. For $\cos\theta_\pi \sim 1$, $m_{\psi(2S)\pi^-}$ is near its maximum value, and $m^2_{\psi\pi}$ is related linearly to $\cos\theta_\pi$, and so it is not surprising that the sideband subtracted distributions of Fig. 30(b) and Fig. 30(d) bear a strong shape resemblance to the corresponding $m_{\psi(2S)\pi^-}$ distributions of Fig. 27(a) and Fig. 27(b), respectively. We note also that the increase in the sideband distribution of Fig. 30(c) towards

TABLE IV: Summary of $m_{\psi(2S)\pi^-}$ data from regions A, C, and E, combined (Fig. 28) for Belle and *BABAR* in the mass range 3.9-4.71 GeV/c^2.

Category	Belle [Fig. 28(a)]	*BABAR* [Fig. 28(b)]
Total signal region events (N)	824 ± 29	786 ± 28
Sideband contribution (B)	172 ± 9	234 ± 15
B/N	21.5%	29.8%
Net signal	652 ± 30	552 ± 32

$\cos\theta_\pi \sim -1$ corresponds to the increase in Fig. 30(b) toward $\psi\pi^-$ threshold. Figure 30 illustrates how important it is to take into account the angular structure in the $K\pi^-$ system in creating the shape of the associated $\psi\pi^-$ mass distribution, even after the removal of the K^* regions.

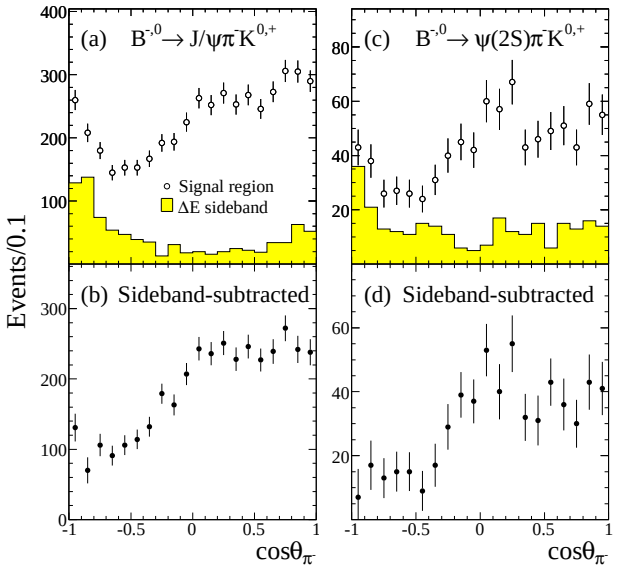

FIG. 30: The $\cos\theta_\pi$ distributions for the combined $K\pi^-$ mass regions A, C, and E, (a), (b) for the decay modes $B^{-,0} \to J/\psi\pi^- K^{0,+}$, and (c), (d) for $B^{-,0} \to \psi(2S)\pi^- K^{0,+}$. In (a) and (c), the points represent the data in the signal region, and the shaded histograms show the ΔE sideband events. In (b) and (d), the signal region distributions are shown after sideband subtraction. No efficiency correction is applied to the data.

XI. FITS TO THE CORRECTED $\psi\pi^-$ MASS DISTRIBUTIONS

A. The fit results

In Fig. 31 we show the results of the fits to the corrected *BABAR* data of Figs. 20(a),(b), Figs. 26(a),(b), and Figs. 27(a),(b). In each fit, the $K\pi^-$ background distribution has been multiplied by a free normalization parameter; an S-wave BW line shape, with free normalization, mass and width parameters, has been added incoherently in order to quantify the search for a $Z(4430)^-$ signal. In each figure, the solid curve represents the fit result; the parameter values for the corresponding $Z(4430)^-$ signal are summarized in Table V. Table V also contains the results obtained when the mass of the $Z(4430)^-$ is fixed (4.433 GeV/c^2), and when both the mass and width (45 MeV) are fixed [5]. For all fits, χ^2/NDF is acceptable, but deteriorates slightly, or fails to improve, as first the mass is fixed and then the mass and width are fixed. We start each fit at the mass and width values of $m = 4.433$ GeV/c^2 and $\Gamma = 45$ MeV.

For the fit to the $J/\psi\pi^-$ mass distribution using the K^*-veto sample with mass and width free, the obtained mass is ~ 100 MeV/c^2 larger than that of the $Z(4430)^-$, the width is essentially undetermined, the signal is more than 2σ negative, and it remains at least 1σ negative for the other fits.

For the K^* region, the fitted mass value is closer to that of the $Z(4430)^-$, but otherwise the results are very similar to those for the K^*-veto region in that negative signal values are obtained.

For the total sample, the results are no better. The signal is negative by $\sim 2.1\sigma$, and remains negative by at least 2σ as the constraints are applied.

We conclude that there is no evidence for $Z(4430)^-$ production via the decay sequence $B^{-,0} \to Z(4430)^- K^{0,+}$, $Z(4430)^- \to J/\psi\pi^-$.

For the fit to the $\psi(2S)\pi^-$ K^*-veto sample (which is equivalent to the Belle analysis sample, but sideband-

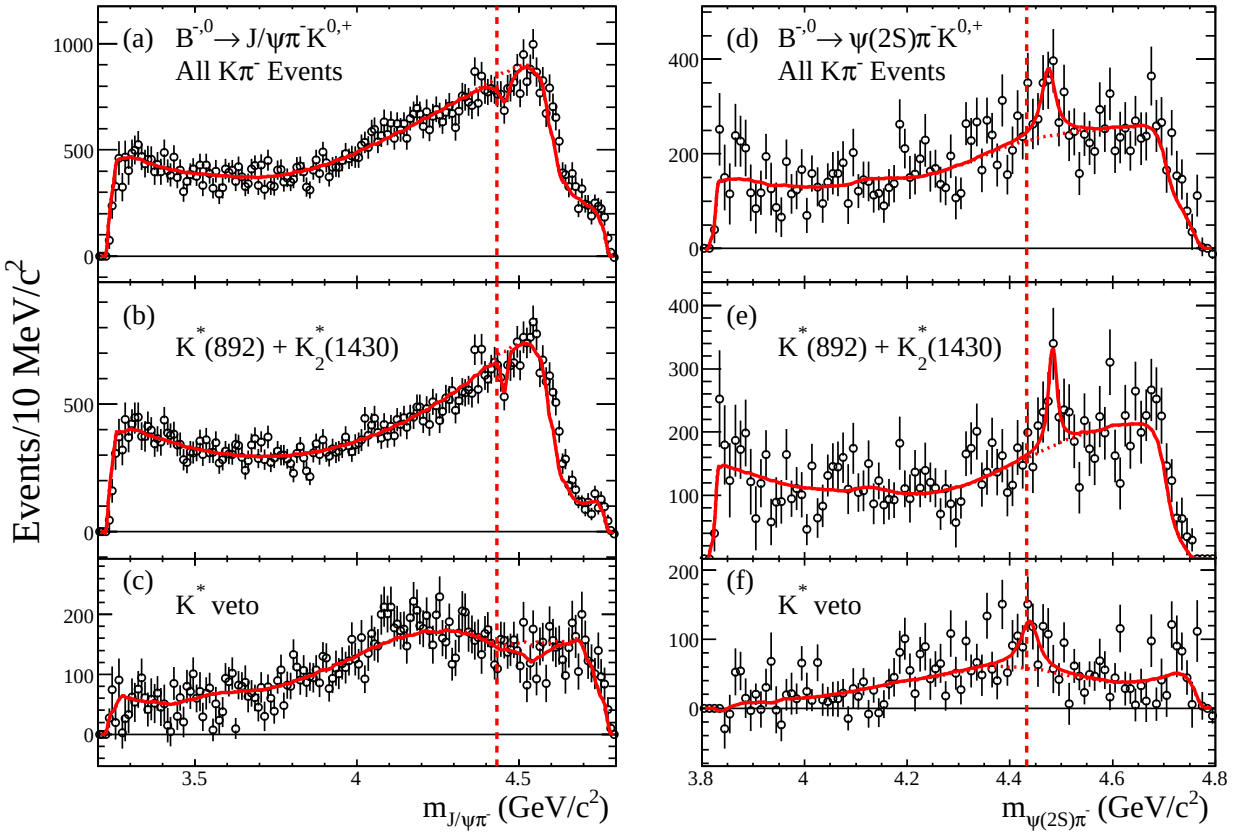

FIG. 31: The results of the fits to the corrected mass distributions, (a)-(c) for $J/\psi\pi^-$, and (d)-(f) for $\psi(2S)\pi^-$. In each figure, the open dots represent the data, and the solid curve represents the fit function, which consists of the $K\pi^-$ background distribution with normalization free, and a relativistic S-wave BW line shape, with mass, width, and normalization free; the dotted curves indicate the $K\pi^-$ background functions; the dashed vertical lines indicate $m_{\psi\pi^-} = 4.433$ GeV/c^2.

subtracted and efficiency-corrected), we obtain mass and width values which are consistent with theirs, but a positive signal which is only $\sim 1.9\sigma$ from zero; fixing mass and width increases this to only $\sim 3.1\sigma$. Since our efficiency in the $Z(4430)^-$ region is almost constant (*cf.* Fig. 23(f)), our corrected signal size with mass and width free (426 ± 229 events) corresponds to $\sim 61 \pm 33$ observed events. This converts to a signal of ~ 70 events in Fig. 29(b), and we estimate a similar value for the Belle distribution of Fig. 29(a). The signal size reported in Ref. [5] is ~ 120 events, obtained on the basis of a background description which ignores $K\pi^-$ mass and angular structures. It is interesting that we find a small positive signal with mass and width consistent with the Belle values. However, with the present small data sample, it seems impossible to decide whether this is due to the production of a real state, or to the imprecision of the normalized $K\pi^-$ moments, primarily in the region between the two K^*'s.

For the K^* region, our fitted mass value is ~ 50 MeV/c^2 higher than the Belle value, and the signal deviates from zero only by $\sim 2.5\sigma$; the imposition of Belle mass and width values yields a signal which is less than $\sim 0.5\sigma$ from zero.

We note that each of these regions corresponds to approximately half of the $\cos\theta_{\psi(2S)}$ range (*cf.* Fig. 21(d)), so that for a flat $Z(4430)^-$ angular distribution, we would expect naively that the signal size for each region would be the same. The values in Table V are consistent with this, however the central mass values differ by ~ 5 standard deviations. Although there could be significant interference effects associated with the K^* regions, it does not seem possible that these could cause the signal to be displaced by approximately one full-width. This, together with the fact that both signals are in the 2-3 standard deviation range, suggests that a more likely interpretation is that both are simply statistical fluctuations.

Finally, for the complete sample, our fitted mass value is ~ 40 MeV/c^2 higher than the Belle value; the width is consistent with Belle's, but the signal size is only $\sim 2.7\sigma$ from zero; this is reduced to $\sim 2.1\sigma$ when the Belle parameters are imposed.

We conclude that there is no convincing evidence for production of the $Z(4430)^-$ state via the decay sequence $B^{-,0} \to Z(4430)^- K^{0,+}$, $Z(4430)^- \to \psi(2S)\pi^-$, especially since the fits take no account of the $K\pi^-$ background un-

certainty associated with the normalized $K\pi^-$ moments.

B. Can the $K\pi^-$ background absorb a $Z(4430)^-$ signal?

Since our evidence for the existence of a $Z(4430)^-$ signal in the $B^{-,0} \to \psi(2S)\pi^- K^{0,+}$ data sample is less than compelling, it is reasonable to ask whether our use of the normalized $K\pi^-$ moments to modulate the $\psi(2S)\pi^-$ background shape might have removed part, or all, of a real $Z(4430)^-$ signal.

Firstly, our $K\pi^-$ background curves in Figs. 20, 26, and 27 show no tendency to peak in a narrow region around the $Z(4430)^-$ mass position, indicated by the dashed vertical line in each figure. Secondly, for the $\psi(2S)\pi^-$ distributions in these figures, the dot-dashed curves obtained using the normalized $K\pi^-$ moments from the $B^{-,0} \to J/\psi\pi^- K^{0,+}$ modes, for which there is no $Z(4430)^-$ signal, do not differ significantly in shape in the signal region from the solid curves from the $B^{-,0} \to \psi(2S)\pi^- K^{0,+}$ modes. Finally, in Ref. [5] it is stated that it is not possible to create a narrow peak from the S-,P-, and D-wave amplitude structure of the $K\pi^-$ system. We agree with this statement and provide a quantitative demonstration below. However, we first show how a $Z(4430)^-$ signal would affect the $\cos\theta_K$ versus $m_{K\pi^-}$ Dalitz plot.

To this end, we have generated a MC sample of events corresponding to $B^{-,0} \to Z(4430)^- K^{0,+}$, $Z(4430)^- \to \psi(2S)\pi^-$ where the $Z(4430)^-$ has the Belle central mass and width values, and decays isotropically. Figure 32 shows the Dalitz plot which results. The $Z(4430)^-$ events yield a narrow locus confined almost entirely to the region $\cos\theta_K < 0$.

For the Legendre polynomials which we have used to modulate the $K\pi^-$ angular distribution, such a distribution yields the following behavior:

- $P_1(\cos\theta_K)$ is almost always negative;
- $P_2(\cos\theta_K)$, which is negative for $|\cos\theta_K| < 0.58$, is negative for $\sim 0.75 < m_{K\pi} < 1.55$ GeV/c^2 *i.e.* almost always;
- $P_3(\cos\theta_K)$, which is positive for $-0.78 < \cos\theta_K < 0$, is positive over almost the entire $m_{K\pi^-}$ range above 1.2 GeV/c^2, which is where we make use of $P_3(\cos\theta_K)$ in the data;
- $P_4(\cos\theta_K)$, which is positive for $|\cos\theta_K| < 0.33$ and $|\cos\theta_K| > 0.88$, is mainly positive for $m_{K\pi^-} > 1.2$ GeV/c^2.

We estimate the effect of such a $Z(4430)^-$ signal on our $K\pi^-$ background by adding a MC-generated $Z(4430)^-$ signal incoherently to the corrected $\psi(2S)\pi^-$ data of Fig. 20(b), and subjecting this new sample to the procedure for creating our $K\pi^-$ background contribution to

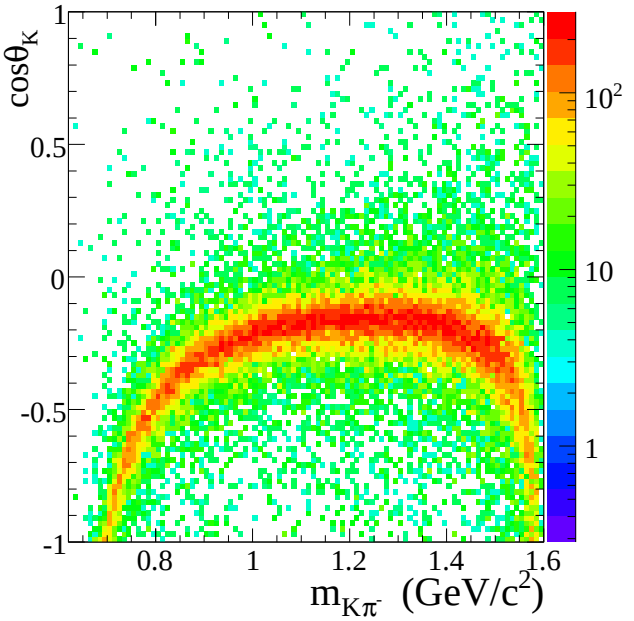

FIG. 32: The $\cos\theta_K$ versus $m_{K\pi^-}$ rectangular Dalitz plot for the $B^{-,0} \to Z(4430)^- K^{0,+}$, $Z(4430)^- \to \psi(2S)\pi^-$ MC events generated using $m_Z = 4.433$ GeV/c^2, $\Gamma_Z = 0.045$ GeV, and with isotropic $Z(4430)^-$ decay.

the $\psi(2S)\pi^-$ mass distribution. As for Fig. 32, we use $m_Z = 4433$ MeV/c^2 and $\Gamma_Z = 45$ MeV in the simulation, and generate a flat $\cos\theta_\psi$ angular distribution. On the basis of the Belle result, we would expect an observed signal of ~ 200 events for the full $\cos\theta_\psi$ angular range (*cf.* Fig. 21(d)), and this would yield an efficiency-corrected signal of ~ 1500 events (*cf.* Fig. 23(f)). Consequently, we generate 1500 events, of which 1493 events are within the ($m_{\rm ES}$, ΔE) signal region. The $m_{\psi(2S)\pi^-}$ distribution for these events is shown as the shaded histogram of Fig. 33(a); the points with error bars show the result of combining these MC events with our corrected $\psi(2S)\pi^-$ data distribution (Fig. 20(b)). The $m_{K\pi^-}$ distribution for this combined sample is shown in Fig. 33(b), where the solid curve shows the result of a fit to the combined data, and the shaded histogram indicates the reflection of the $Z(4430)^-$ MC events. We use this new fit curve to generate 10 million events corresponding to $B^{-,0} \to \psi(2S)\pi^- K^{0,+}$ as before, and normalize this sample to the combined data and MC-generated $Z(4430)^-$ sample. We add the unnormalized $K\pi^-$ moments for the simulated $Z(4430)^-$ events to the corrected $K\pi^-$ data moments, and use the distribution of Fig. 33(b) to create new normalized $K\pi^-$ moments as in Sec. IX. Finally, we follow the weighting procedure described in Sec. IX to create the new $K\pi^-$ background description shown by the dashed curve of Fig. 34 in comparison to the combined $m_{\psi(2S)\pi^-}$ distribution of Fig. 33(a).

Clearly, this dashed curve does not describe the $Z(4430)^-$ signal region. However, the shape of the curve

TABLE V: Results of the fits to the corrected *BABAR* $\psi\pi^-$ mass distributions; all fits use the relevant *BABAR* $K\pi^-$ background shape.

Type of fit	total	K^* region	K^* veto
$J/\psi\pi^-$ sample;	$m = 4455 \pm 8$ MeV/c^2	$m = 4454 \pm 4$ MeV/c^2	$m = 4545 \pm 30$ MeV/c^2
$Z(4430)^-$ mass and width free	$\Gamma = 42 \pm 27$ MeV	$\Gamma = 17 \pm 12$ MeV	$\Gamma = 100 \pm 96$ MeV
	$N_Z = -901 \pm 420$	$N_Z = -514 \pm 223$	$N_Z = -411 \pm 181$
	$\chi^2/NDF = 131/154$	$\chi^2/NDF = 135/154$	$\chi^2/NDF = 159/154$
$J/\psi\pi^-$ sample;	$\Gamma = 82 \pm 77$ MeV	$\Gamma = 79 \pm 39$ MeV	$\Gamma = 10 \pm 12$ MeV
$Z(4430)^-$ fixed mass and free width	$N_Z = -1098 \pm 490$	$N_Z = -810 \pm 393$	$N_Z = -86 \pm 64$
	$\chi^2/NDF = 136/155$	$\chi^2/NDF = 143/155$	$\chi^2/NDF = 162/155$
$J/\psi\pi^-$ sample;	$N_Z = -704 \pm 249$	$N_Z = -540 \pm 225$	$N_Z = -147 \pm 105$
$Z(4430)^-$ fixed mass and width	$\chi^2/NDF = 137/156$	$\chi^2/NDF = 144/156$	$\chi^2/NDF = 164/156$
$\psi(2S)\pi^-$ sample;	$m = 4476 \pm 8$ MeV/c^2	$m = 4483 \pm 3$ MeV/c^2	$m = 4439 \pm 8$ MeV/c^2
$Z(4430)^-$ mass and width free	$\Gamma = 32 \pm 16$ MeV	$\Gamma = 17 \pm 12$ MeV	$\Gamma = 41 \pm 33$ MeV
	$N_Z = 703 \pm 260$	$N_Z = 447 \pm 177$	$N_Z = 426 \pm 229$
	$\chi^2/NDF = 93/96$	$\chi^2/NDF = 91/96$	$\chi^2/NDF = 106/96$
$\psi(2S)\pi^-$ sample;	$\Gamma = 97 \pm 77$ MeV	$\Gamma = 100 \pm 82$ MeV	$\Gamma = 36 \pm 26$ MeV
$Z(4430)^-$ fixed mass and free width	$N_Z = 710 \pm 440$	$N_Z = 246 \pm 247$	$N_Z = 414 \pm 194$
	$\chi^2/NDF = 101/97$	$\chi^2/NDF = 102/97$	$\chi^2/NDF = 107/97$
$\psi(2S)\pi^-$ sample;	$N_Z = 440 \pm 212$	$N_Z = 89 \pm 162$	$N_Z = 431 \pm 137$
$Z(4430)^-$ fixed mass and width	$\chi^2/NDF = 101/98$	$\chi^2/NDF = 101/98$	$\chi^2/NDF = 107/98$

has been changed compared to that of Fig. 20(b) because of the effect of the $Z(4430)^-$ signal events on the low-order Legendre polynomial $K\pi^-$ moments. This is shown by the shaded histogram in Fig. 34, which represents the difference between the dashed curve in this figure and the solid curve in Fig. 20(b).

A complete representation of the highly localized $Z(4430)^-$ distribution in Fig. 32 requires the use of Legendre polynomials to order more than 30, and so our low-order representation of the $K\pi^-$ angular structure is unable to do this. The shaded histogram does reach a maximum at about the $Z(4430)^-$ mass value, but corresponds to a width of ~ 160 MeV, which is almost four times larger than the input signal value.

A fit to the distribution of Fig. 34 with the normalization of the new $K\pi^-$ background, and the normalization, mass and width of the $Z(4430)^-$ signal, free yields $m_{Z(4430)^-} = 4433 \pm 3$ MeV/c^2, $\Gamma_{Z(4430)^-} = 34 \pm 12$ MeV, and $N_{Z(4430)^-} = 1402 \pm 315$ events so that the width is reduced to $\sim 75\%$, and the signal to $\sim 94\%$, of the input

value, while the mass is essentially unchanged. The solid curve in Fig. 34 represents the fit result, and the dotted curve shows the reduced level of $K\pi^-$ background. If the $Z(4430)^-$ width is fixed to 45 MeV, we obtain $N_{Z(4430)^-} = 1558 \pm 220$ events. This is consistent with the input value, and presumably more properly reflects the effect of the statistical uncertainties in the underlying data distribution. We therefore use this to estimate the magnitude of the systematic signal reduction factor, and so obtain a value of $\sim 90\%$.

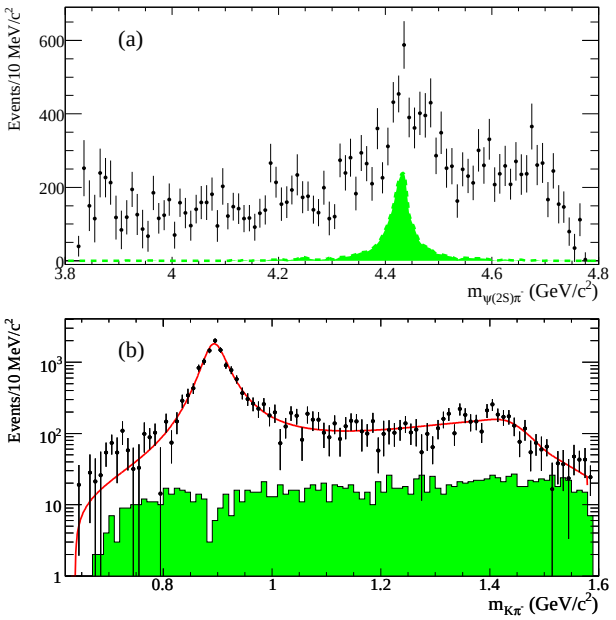

FIG. 33: (a): The combined $m_{\psi(2S)\pi^-}$ mass distribution for the data of Fig. 20(b) and the MC $Z(4430)^-$ sample generated as described in the text; the shaded histogram represents the MC sample; (b) the $K\pi^-$ mass distribution corresponding to Fig. 33(a); the shaded histogram represents the reflection of the MC $Z(4430)^-$ events, and the curve shows the result of the fit.

This is a direct demonstration in support of the statement in the Belle letter [5] that a narrow peak in the $\psi\pi^-$ mass distribution cannot be generated by only S-, P-, and D-wave amplitudes in the $K\pi^-$ system, and indicates that our use of low-order Legendre polynomials in creating our $K\pi^-$ background could lead to an approximately 10% systematic reduction of a narrow $Z(4430)^-$ signal of the reported magnitude.

C. Branching fractions

In Table VI, we summarize the branching fraction values and their 95% c.l. upper limits, obtained for the individual B decay modes studied in the present analysis by repeating the fits of Figs. 31(a) and 31(d), but with $Z(4430)^-$ mass and width fixed to the central values obtained by Belle. The errors quoted are statistical, and

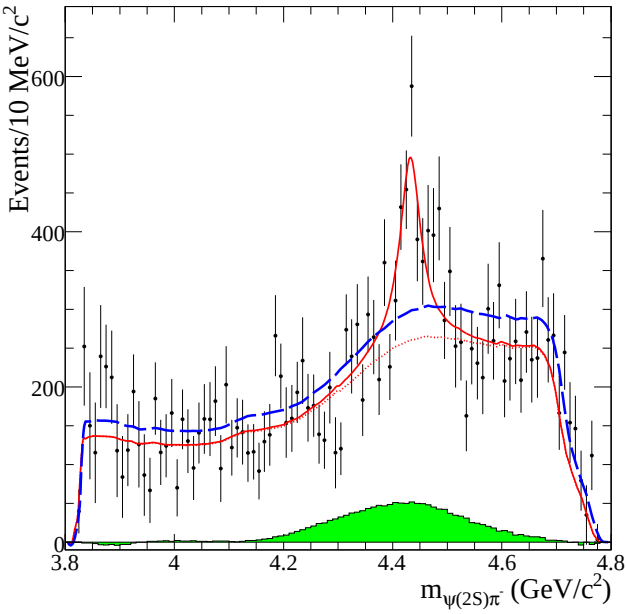

FIG. 34: The $m_{\psi(2S)\pi^-}$ distribution of Fig. 33(a) for the data and MC samples combined as described in the text. The dashed curve represents the $K\pi^-$ background distribution, obtained as described in the text, and the shaded histogram represents the difference between this dashed curve and the solid curve of Fig. 20(b), *i.e.* it represents the impact of the MC $Z(4430)^-$ signal. The solid curve is the result of a fit using the $K\pi^-$ background function and a relativistic S-wave BW, and the dotted curve shows the resulting renormalized dashed curve.

the upper limits were obtained using these values. For the $\psi(2S)\pi^-$ modes, the branching-fraction and upper-limit values have been increased by 10% in order to take account of possible reduction of $Z(4430)^-$ signal size, as described in Sec. XI B.

The branching fraction for the decay mode $B^0 \to Z(4430)^- K^+, Z(4430)^- \to \psi(2S)\pi^-$ from Belle is $(4.1 \pm 1.0 \pm 1.4) \times 10^{-5}$, to be compared to our upper limit of 3.1×10^{-5} at 95% c.l.

XII. SUMMARY AND CONCLUSIONS

We have searched for evidence supporting the existence of the $Z(4430)^-$ in the $\psi\pi^-$ mass distributions resulting from the decays $B^{-,0} \to \psi\pi^- K^{0,+}$ in a large data sample recorded by the *BABAR* detector at the PEP-II e^+e^- collider at SLAC. Since the relevant Dalitz plots are dominated by mass and angular distribution structures in the $K\pi^-$ system, we decided to investigate the extent to which the reflections of these features might describe the associated $\psi\pi^-$ mass distributions. To this end, we obtained a detailed description of the mass and angular structures of the $K\pi^-$ system based on the expected underlying S-, P-, and D-wave $K\pi^-$ amplitude contri-

TABLE VI: The $Z(4430)^-$ signal size, the branching fraction value, and its 95% c.l. upper limit for each decay mode; the errors quoted are statistical, and the upper limits were obtained using these values; the $Z(4430)^-$ mass and width have been fixed to the central values obtained by Belle [5].

Decay mode	$Z(4430)^-$ signal	Branching fraction ($\times 10^{-5}$)	Upper limit ($\times 10^{-5}$ at 95% c.l.)
$B^- \to Z(4430)^- \bar{K}^0, Z(4430)^- \to J/\psi\pi^-$	-17 ± 140	-0.1 ± 0.8	1.5
$B^0 \to Z(4430)^- K^+, Z(4430)^- \to J/\psi\pi^-$	-670 ± 203	-1.2 ± 0.4	0.4
$B^- \to Z(4430)^- \bar{K}^0, Z(4430)^- \to \psi(2S)\pi^-$	148 ± 117	2.0 ± 1.7	4.7
$B^0 \to Z(4430)^- K^+, Z(4430)^- \to \psi(2S)\pi^-$	415 ± 170	1.9 ± 0.8	3.1

butions, and in the process even found evidence of $D-F$ wave interference in the J/ψ decay modes. The fractional S-, P-, and D-wave intensity contributions to the corrected $K\pi^-$ mass distributions for $B^- \to J/\psi\pi^- K^0_S$ and $B^0 \to J/\psi\pi^- K^+$ were found to be the same within error, as are the branching fraction values after all corrections, and so we combined these data in our analysis of the $J/\psi\pi^-$ mass distributions. We observed similar features for the corresponding $\psi(2S)$ decay modes, even though the analysis sample is ~ 6.6 times smaller than that for J/ψ (Table II), and we combined the charged and neutral B-meson samples for the $\psi(2S)$ analysis also.

We next investigated the $\psi\pi^-$ mass distributions on the basis of our detailed analysis of the $K\pi^-$ system. We used a MC generator to create large event samples for $B^{-,0} \to \psi\pi^- K^{0,+}$ with $K\pi^-$ mass distribution generated according to the overall fit function obtained from the corrected data, but with a uniform $\cos\theta_K$ distribution. The $\cos\theta_K$ dependence was then modulated using normalized Legendre polynomial moments whose values were obtained from our corrected data by linear interpolation.

The total corrected $J/\psi\pi^-$ mass distribution (Fig. 20(a)) is well described by this $K\pi^-$ background, whose form can be seen more clearly in Fig. 22(a). The residuals (Fig. 20(c)) show no evidence of a $Z(4430)^-$ signal, and this is true also for the various regions of $K\pi^-$ mass shown in Fig. 24(a)-(e), Fig. 26(a),(c), and Fig. 27(a),(c). When we fit the data using a function which allows the presence of a $Z(4430)^-$ signal, we obtain only negative $Z(4430)^-$ signal intensities (Fig. 31(a)-(c), Table V). We find this to be the case also for the B^- and B^0 modes separately, and summarize the corresponding branching fraction upper limits in Table VI for $Z(4430)^-$ mass and width fixed at the central values obtained by Belle [5].

We conclude that there is no evidence to support the existence of a narrow resonant structure in the $J/\psi\pi^-$ mass distributions for our data on the decay modes $B^{0,-} \to J/\psi\pi^- K^{+,0}$.

The corresponding corrected $\psi(2S)\pi^-$ distributions of Figs. 20(b),(d), Figs. 24(f)-(j) and Figs. 25(f)-(j), Figs. 26(b) and (d), and Figs. 27(b) and (d) likewise show no clear evidence of a narrow signal at the $Z(4430)^-$ mass position.

We have directly compared our uncorrected $\psi(2S)\pi^-$ data with K^* veto, to those from Ref. [5]; there is no evidence of statistically significant difference (Fig. 29(c)).

In order to quantify our $Z(4430)^-$ production rate estimates, we fit our total corrected $\psi\pi^-$ mass distributions of Figs. 20(a) and 20(b), using the $K\pi^-$ background shapes shown in these figures, together with a $Z(4430)^-$ line shape. For $J/\psi\pi^-$ we obtain a negative signal, while for $\psi(2S)\pi^-$ we obtain a 2.7 standard deviation signal with fitted width consistent with the value obtained by Belle, but with central mass value ~ 43 MeV/c^2 higher than that reported by Belle, which corresponds to a +4.7 standard deviation difference. These fit results are shown in Figs. 31(a) and 31(d), respectively, and are summarized in Table V. We repeated these fits for the individual decay modes of Eqs.(1)-(4) with $Z(4430)^-$ mass and width fixed to the central values reported by Belle, and obtained the branching fraction and upper limit values summarized in Table VI. In particular, we find a branching fraction upper limit for the process $\mathcal{B}(B^0 \to Z(4430)^- K^+, Z^- \to \psi(2S)\pi^-) < 3.1 \times 10^{-5}$ at 95% c.l., and a corresponding value for the reaction $\mathcal{B}(B^- \to Z(4430)^- \bar{K}^0, Z^- \to \psi(2S)\pi^-) < 4.7 \times 10^{-5}$ at 95% c.l. We conclude that our analyses provide no significant evidence for the existence of the $Z(4430)^-$.

It will be of great interest to see whether or not the $Z(4430)^-$ is confirmed by a future analysis based upon a significantly larger data sample than is available at present.

XIII. ACKNOWLEDGMENTS

We are grateful for the extraordinary contributions of our PEP-II colleagues in achieving the excellent luminosity and machine conditions that have made this work possible. The success of this project also relies critically on the expertise and dedication of the computing organizations that support *BABAR*. The collaborating institutions wish to thank SLAC for its support and the kind hospitality extended to them. This work is supported by the US Department of Energy and National Science Foundation, the Natural Sciences and Engineering Research Council (Canada), the Commissariat à l'Energie Atomique and Institut National de Physique Nucléaire et de Physique des Particules (France), the Bundesministerium für Bildung und Forschung and Deutsche Forschungsgemeinschaft (Germany), the Istituto Nazionale di Fisica Nucleare (Italy), the Foundation for Fundamental Research on Matter (The Netherlands), the Research Council of Norway, the Ministry of Education and Science of the Russian Federation, Ministerio de Educación y Ciencia (Spain), and the Science and Technology Facilities Council (United Kingdom). Individuals have received support from the Marie-Curie IEF program (European Union) and the A. P. Sloan Foundation.

APPENDIX A: THE DALITZ PLOT EFFICIENCY-CORRECTION PROCEDURE

The efficiency is obtained using samples of Monte Carlo events corresponding to the decay processes of Eqs. (1)-(4) generated uniformly over the final state Dalitz plot.

In general, the phase space volume element in the Dalitz plot corresponding to the decay $B \to \psi\pi K$ is given by:

$$d\rho \sim d(m^2_{K\pi}) \cdot d(m^2_{\psi\pi})\,, \tag{A1}$$

where $m_{K\pi^-}$ ($m_{\psi\pi^-}$) is the invariant mass of the $K\pi^-$ ($\psi\pi^-$) system.

However, when the efficiency is studied in such rectilinear area elements, those elements at the plot boundary are partially outside the plot, and this leads to a rather cumbersome efficiency treatment. The phase space volume element of Eq. (A1) may be transformed to

$$d\rho' \sim p \cdot \frac{q}{m_{K\pi}} \cdot m_{K\pi}\, d(m_{K\pi})\, d(\cos\theta_{\rm K})\,, \tag{A2}$$

i.e.

$$d\rho' \sim p \cdot q\, d(m_{K\pi}) d(\cos\theta_{\rm K})\,, \tag{A3}$$

where p is the momentum of the ψ daughter of the B in the B rest frame, and q is the momentum of the K in the rest frame of the $K\pi^-$ system. This expression is such that the phase space density is uniform in $\cos\theta_K$ at a given value of $m_{K\pi^-}$.

The range of $\cos\theta_K$ is [-1,1], and that of $m_{K\pi^-}$ is from threshold to $m_B - m_\psi$, so that the resultant "Dalitz Plot" is rectangular in shape, with the factor $p \cdot q$ representing the Jacobian of the variable transformation. A plot of this kind can then be used readily to study efficiency behavior over the entire phase space region without the problems incurred at the boundary of a conventional Dalitz plot (see, for example, Appendix B of Ref. [22]).

The reconstruction efficiency calculated using the Monte Carlo simulated events is parametrized as a function of $m_{K\pi^-}$ and $\cos\theta_K$, and then used to correct the data by weighting each event by the inverse of its parametrized efficiency value. For a given mass interval $I = [m_{K\pi^-}, m_{K\pi^-} + dm_{K\pi^-}]$, let N be the number of generated events, and let n_{reco}, represent the number of reconstructed events. The generated $\cos\theta_K$ distribution is flat, but in general efficiency effects will cause the reconstructed $\cos\theta_K$ distribution to have structure. Writing the angular distribution in terms of appropriately normalized Legendre polynomials,

$$\frac{dN}{d\cos\theta_K} = N\langle P_0\rangle P_0(\cos\theta_K) \tag{A4}$$

and,

$$\frac{dn_{reco}}{d\cos\theta_K} = n_{reco}\sum_{i=0}^{L}\langle P_i\rangle P_i(\cos\theta_K) \tag{A5}$$

where the normalizations are such that,

$$\int_{-1}^{1} P_i(\cos\theta_K) P_j(\cos\theta_K) d(\cos\theta_K) = \delta_{ij}\,, \tag{A6}$$

where $P_i = \sqrt{2\pi}Y_i^0$, and Y_i^0 is a spherical harmonic function. The value of L is obtained empirically.

Using this orthogonality condition, the coefficients in the expansion are obtained from

$$\langle P_j\rangle = \frac{1}{n_{reco}}\int_{-1}^{1} P_j(\cos\theta_K)\frac{dn_{reco}}{d\cos\theta_K} d(\cos\theta_K)\,, \tag{A7}$$

where the integral is given, to a good approximation for a large enough MC sample, by $\sum_{i=1}^{n_{reco}} P_j(\cos\theta_{K_i})$. The index i runs over the reconstructed events in mass interval I, such that $n_{reco}\langle P_j\rangle \sim \sum_{i=1}^{n_{reco}} P_j(\cos\theta_{K_i})$, and the effect of efficiency loss on the angular distribution is represented through these coefficients. The absolute efficiency, calculated as a function of $\cos\theta_K$ and $m_{K\pi^-}$, in mass interval I, is then given by

$$E(\cos\theta_K, m_{K\pi^-}) = \frac{n_{reco}\left(\sum_{i=0}^{L}\langle P_i\rangle P_i(\cos\theta_K)\right)}{N\langle P_0\rangle P_0(\cos\theta_K)}\,. \tag{A8}$$

With

$$E_0 = \frac{n_{reco}}{N} \tag{A9}$$

and

$$E_j = 2\frac{n_{reco}\langle P_j\rangle}{N} = 2\frac{\sum_{i=1}^{n_{reco}} P_j(\cos\theta_{K_i})}{N}, \quad \text{(A10)}$$

for a large enough sample (note that the factor 2 enters since $\langle P_0\rangle P_0(\cos\theta_K) = 1/2$), Eq. (A8) becomes,

$$E(\cos\theta_K, m_{K\pi^-}) = E_0 + E_1 P_1(\cos\theta_K) + ... + E_L P_L(\cos\theta_K)\,. \quad \text{(A11)}$$

The mean value of the $P_j(\cos\theta_{K_i})$, with $i = 1, ..., n_{reco}$, corresponding to mass interval I, is written as $\langle P_j\rangle$. The r.m.s. deviation of the $P_j(\cos\theta_{K_i})$ w.r.t. $\langle P_j\rangle$, σ, is given by

$$\sigma^2 = \sum_{i=1}^{n_{reco}} \frac{\left(P_j(\cos\theta_{K_i}) - \langle P_j\rangle\right)^2}{n_{reco} - 1}\,. \quad \text{(A12)}$$

The error on the mean is then $\delta\langle P_j\rangle = \frac{\sigma}{\sqrt{n_{reco}}}$ and from Eq. (A12),

$$\delta\langle P_j\rangle = \sqrt{\frac{\sum_{i=1}^{n_{reco}} \left(P_j(\cos\theta_{K_i}) - \langle P_j\rangle\right)^2}{n_{reco}(n_{reco}-1)}} = \sqrt{\frac{\left[\sum_{i=1}^{n_{reco}} \frac{\left(P_j(\cos\theta_{K_i})\right)^2}{n_{reco}}\right] - \langle P_j\rangle^2}{n_{reco}-1}}\,. \quad \text{(A13)}$$

The uncertainty in the parameter $E_0 = \frac{n_{reco}}{N}$ is given by:

$$\delta(E_0) = E_0\sqrt{\frac{1}{n_{reco}} + \frac{1}{N}}\,, \quad \text{(A14)}$$

and the uncertainty in the coefficient E_j is given by:

$$\delta(E_j) = \frac{2}{N}\cdot \sqrt{\sum_{i=1}^{n_{reco}} \left(P_j(\cos\theta_{K_i})\right)^2 + \frac{\left(\sum_{i=1}^{n_{reco}} \left(P_j(\cos\theta_{K_i})\right)\right)^2}{N}}\,. \quad \text{(A15)}$$

For each of the processes represented by Eqs.(1)-(4), the efficiency analysis is carried out in 50 MeV/c^2 $K\pi^-$ mass intervals from threshold to the maximum value accessible. As shown in Sec. VI, Fig. 7, the $K\pi^-$ mass dependence of the average efficiency parameter, E_0, depends on the decay mode of the ψ involved, and so is obtained by using the MC sample for that particular decay mode. The angular dependence represented by E_1, E_2,...*etc.* does not depend on the individual ψ decay mode, and so these coefficients are calculated by combining the MC samples for the individual ψ modes. For the B meson decay processes of Eqs. (1)- (4), the main features of the angular dependence of the efficiency are very similar, and so we present the results only for $B^0 \to \psi(2S)\pi^- K^+$ by way of illustration.

Simulated MC events are subjected to the same reconstruction and event-selection procedures as those applied to the data. For the process of Eq. (4), the $\cos\theta_K$ distributions for the surviving MC events are shown for each $K\pi^-$ mass interval in Fig. 35. We chose a small interval size (0.02) in order to investigate the significant decrease in efficiency observed for $\cos\theta_K \sim +1$ and $0.720 < m_{K\pi^-} < 0.920$ GeV/c^2 (Figs. 35(c)-(f)) and for $\cos\theta_K \sim -1$ and $0.970 < m_{K\pi^-} < 1.270$ GeV/c^2 (Figs. 35(h)-(m)). Representation of such localized losses requires the use of high-order Legendre polynomials; we find that $L = 12$ yields a satisfactory description, as demonstrated by the curves in Fig. 35. The $K\pi^-$ mass dependence of the resulting values of E_1 - E_{12} is shown in Fig. 36, and is parametrized in each case by the fifth-order polynomial curve shown. These parameterizations, together with those describing the $K\pi^-$ mass dependence of E_0 for the individual ψ decay modes (Sec. VI) enable us to calculate the efficiency at any point in the relevant rectangular Dalitz plot, and hence for each event in the corresponding data sample. We then assign to each event a weight given by the inverse of this efficiency value, and by using this weight are able to create efficiency-corrected distributions.

As discussed in Sec. VI, the efficiency loss for $\cos\theta_K \sim +1$ is due to the failure to reconstruct low momentum charged pions in the laboratory frame, while that for $\cos\theta_K \sim -1$ is due to the similar loss of low momentum kaons (Fig. 9).

[1] M. Gell-Mann, Baryons And Mesons," Phys. Lett. **8**, 214 (1964).
[2] G. Trilling, J. Phys. G **33**, 1019 (2006).
[3] C. Amsler *et al.* [Particle Data Group], Phys. Lett. **B667**, 1 (2008).
[4] L. Maiani *et al.*, Phys. Rev. D **71**, 014028 (2005); L. Maiani *et al.*, Phys. Rev. D **72**, 031502(R) (2005); L. Maiani, A.D. Polosa, and V. Riquer, Phys. Rev. Lett. **99**, 182003 (2007).
[5] S.-K. Choi *et al.* [Belle Collaboration], Phys. Rev. Lett. **100**, 142001 (2008).
[6] The use of charge conjugate reactions is implied throughout this paper.
[7] L. Maiani, A.D. Polosa, and V. Riquer, New Journal of Physics, **10**, 073004 (2008).
[8] M. Karliner and H. J. Lipkin, Phys. Lett. B **638**, 221

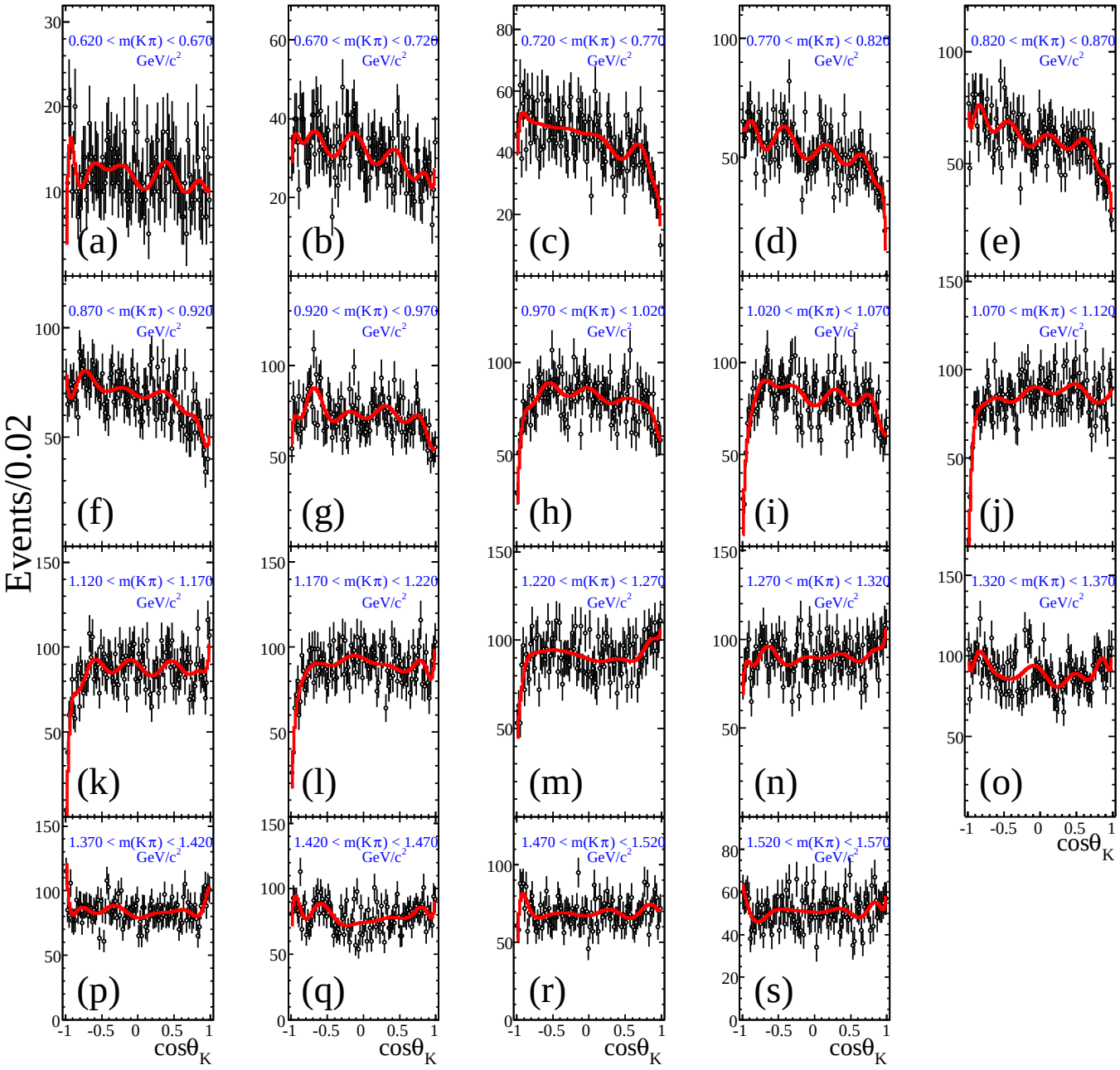

FIG. 35: The $\cos\theta_K$ distributions in 50 MeV/c^2 $K\pi^-$ mass intervals for the decay mode $B^0 \to \psi(2S)\pi^- K^+$. The points represent the data, and the curves show the functions calculated from the moments.

(2006); Ce Meng and Kuang-Ta Chao, arXiv:0708.4222 [hep-ph]; J. L. Rosner, Phys. Rev. D **76**, 114002 (2007); M. Karliner and H. J. Lipkin, arXiv:0802.0649 [hep-ph].

[9] We use "ψ" to represent "J/ψ or $\psi(2S)$" unless these are required explicitly.

[10] B. Aubert *et al.* [*BABAR* Collaboration], Nucl. Instrum. Meth. A **479**, 1 (2002).

[11] W. Menges, Nuclear Science Symposium Conference Record, 2005 IEEE, **3**, 1470 (2005).

[12] H. Albrecht *et al.* [ARGUS Collaboration], Z. Phys. C **48**, 543 (1990).

[13] B. Aubert *et al.* [*BABAR* Collaboration], Phys. Rev. Lett. **87**, 241801 (2001).

[14] B. Aubert *et al.* [*BABAR* Collaboration], Phys. Rev. D **71**, 032005 (2005).

[15] J. M. Blatt and V. F. Weisskopf, *Theoretical Nuclear Physics*, John Wiley and Sons (1952).

[16] D. Aston *et al.* [LASS Collaboration], Nucl. Phys. **B296**, 493 (1988); W. Dunwoodie, private communication.

[17] S. T'Jampens, Ph.D. Thesis, Université Paris XI (2002);

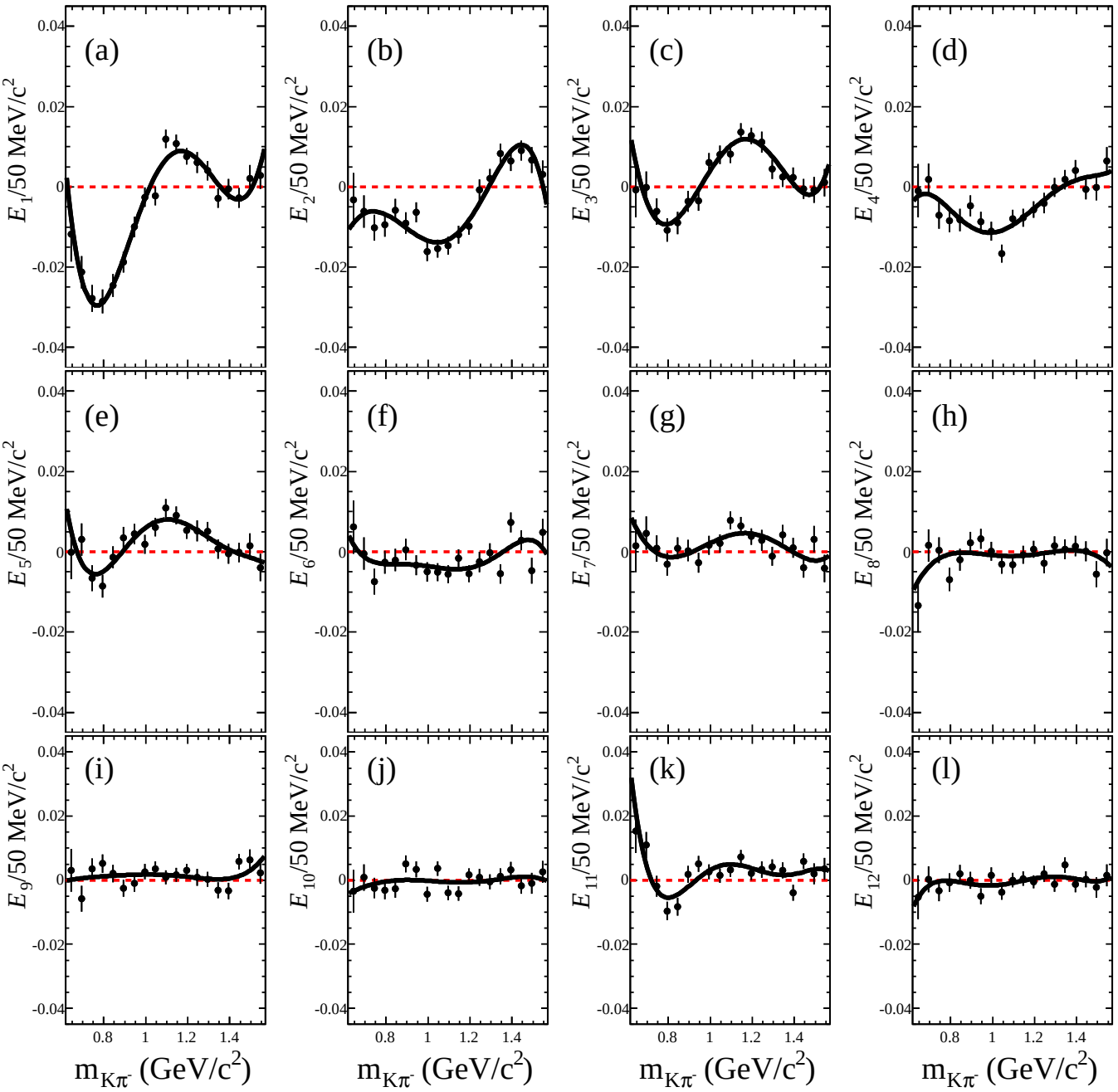

FIG. 36: The $K\pi^-$ mass dependence of the coefficients E_1 through E_{12} for the decay mode $B^0 \to \psi(2S)\pi^- K^+$. The points show the calculated values, and the curves result from fits to the data using a fifth-order polynomial.

SLAC-R-836, Appendix D.
[18] E. M. Aitala *et al.* [E791 Collaboration], Phys. Rev. D **73**, 032004 (2006) [Erratum-ibid. D **74**, 059901 (2006)].
[19] B. Aubert *et al.* [*BABAR* Collaboration], Phys. Rev. D **76**, 031102(R) (2007).
[20] We have verified that the difference in the Lorentz boost between the *BABAR* and Belle experiments does not significantly affect these losses of low-momentum particles.
[21] We thank the Belle Collaboration for allowing us to reproduce the histograms in Fig. 2 of Ref. [5].
[22] V. Ziegler, Ph.D. Thesis, SLAC-R-868 (2007).